

## ORIGINAL ARTICLE

# *In vivo* high-efficiency targeted photodynamic therapy of ultra-small Fe<sub>3</sub>O<sub>4</sub>@polymer-NPO/PEG-Glc@Ce6 nanoprob es based on small size effect

Ting Yin<sup>1</sup>, Qian Zhang<sup>1</sup>, Haigang Wu<sup>2</sup>, Guo Gao<sup>1</sup>, Joseph G Shapter<sup>3</sup>, Yulan Shen<sup>4</sup>, Qiaozhi He<sup>1</sup>, Peng Huang<sup>1</sup>, Wen Qi<sup>1</sup> and Daxiang Cui<sup>1</sup>

Effectively prolonging the residence time of nanoprob es in the tumor region and reducing the accumulation of nanoprob es in the vital organs (for example, lung, liver and spleen) is crucial for high-efficiency photodynamic therapy (PDT) of cancer. Herein, we systematically report an ultra-small and highly stable nanoplatform with diameters of 4, 8 and 13 nm that exhibited excellent photodynamic therapeutic efficacy using Fe<sub>3</sub>O<sub>4</sub>@polymer-NPO/PEG-Glc@Ce6 nanoprob es. Based on the small size effect, the nanoprob es displayed lower cytotoxicity and excellent biocompatibility. Owing to the synergistic virtues of markedly active targeting and intrinsic small size effect, the Fe<sub>3</sub>O<sub>4</sub>@P-NPO/PEG-Glc@Ce6 nanoprob es can effectively prolong their residence time in the tumor region and reduce accumulation in the normal organs. Benefitting from the small size effect, the synthesized Fe<sub>3</sub>O<sub>4</sub>@P-NPO/PEG-Glc@Ce6 nanoprob es exhibited excellent tumor-targeting capability and photodynamic therapeutic efficacy by inhibiting the growth of tumors in mice under visible red light irradiation with a relatively lower power. The successful application of the small size effect in Fe<sub>3</sub>O<sub>4</sub>@P-NPO/PEG-Glc@Ce6 nanoprob es to significantly improve the PDT efficiency in our strategy suggests new building blocks for PDT of tumors and paves a new way for clinical therapies and translation in the near future.

NPG Asia Materials (2017) 9, e383; doi:10.1038/am.2017.68; published online 26 May 2017

## INTRODUCTION

To further enhance drug retention in tumor tissues and decrease toxicity to vital organs *in vivo*, the development of multifunctional integrated nanoparticle systems for effective cancer diagnosis/treatment has been extensively studied in the past few years.<sup>1,2</sup> Among them, photodynamic therapy (PDT) is one promising and effective strategy for clinical therapies because near-infrared light is used as an external stimulus, which has many merits, such as simple operation, easy focusing on a targeted region, and the lowest damage to peripheral normal skin and tissues.<sup>3</sup> In the presence of photosensitizer molecules, near-infrared light can effectively stimulate these agents and thereafter generate singlet oxygen to enhance irreversible damage to tumor cells.<sup>4</sup> Furthermore, the application of singlet oxygen to directly kill cancer cells is a noninvasive and repeatable therapy for cancer.<sup>5</sup> However, some intrinsic obstacles of free photosensitizers, such as photostability, water-insolubility and poor pharmacokinetics, and especially the poor targeting accumulation in tumor tissues, has hindered the clinical application of PDT in the past few years.<sup>6</sup> Therefore, the development of an effective strategy to improve the

targeting efficiency of photosensitizers to tumor tissues is highly desired.

To date, many nanoplatforms, such as gold nanoclusters,<sup>7,8</sup> carbon nanomaterials,<sup>9,10</sup> quantum dots<sup>11</sup> and upconversion nanomaterials<sup>12,13</sup> have been explored as the carriers of photosensitizers for PDT. However, medical translation of the traditional nanoplatforms has been hindered owing to the high toxicity and low efficiency of PDT. Recent studies have shown that magnetic nanoparticles (MNPs, that is, low toxicity, excellent biocompatibility and a unique magnetic-response property) could act as the most promising nanoplatform for enhancing PDT efficacy in fighting cancer.<sup>14</sup> Generally, the surface of MNPs is covered by a functional layer. This improves the stability of MNPs and provides active sites for the desired applications. Dendrimers, as a unique structural family, have attracted great interest.<sup>15</sup> The highly hydrophobic segments of dendrimers can be applied to effectively encapsulate and deliver limited-solubility anticancer drugs for therapeutic applications.<sup>16–18</sup> The hydrophilic end groups in dendrimers present high biocompatibility and water-solubility. The monomer structure of

<sup>1</sup>Institute of Nano Biomedicine and Engineering, Shanghai Engineering Research Center for Intelligent Diagnosis and Treatment Instrument, Department of Instrument Science and Engineering, Department of Micro/Nano Electronics, School of Electronic Information and Electrical Engineering, Shanghai Jiao Tong University, Shanghai, China; <sup>2</sup>School of Biomedical Engineering, Shanghai Jiao Tong University, Shanghai, China; <sup>3</sup>School of Chemical and Physical Sciences, Flinders University, Bedford Park, Adelaide, SA, Australia and <sup>4</sup>Department of Radiology, Shanghai Jiao Tong University Affiliated Sixth People's Hospital, Shanghai Jiao Tong University, Shanghai, China

Correspondence: Professor G Gao and Professor D Cui, Institute of Nano Biomedicine and Engineering, Shanghai Engineering Research Center for Intelligent Diagnosis and Treatment Instrument, Department of Instrument Science and Engineering, Department of Micro/Nano Electronics, School of Electronic Information and Electrical Engineering, Shanghai Jiao Tong University, 800 Dongchuan Road, Shanghai 200240, China.  
E-mail: guogao@sjtu.edu.cn or dx cui@sjtu.edu.cn

Received 6 December 2016; revised 6 March 2017; accepted 13 March 2017

dendrimers is similar to that of PEG, which can also prolong circulation time in the biosystem and enhance retention in the malignant tumor region via an enhanced permeability and retention effect.<sup>19,20</sup> These outstanding characteristics of dendrimers make them a desired nanosystem for cancer theranostics. However, MNPs/dendrimer-based theranostic nanoplateforms with multifunctional imaging and therapeutic functionalities have rarely been reported, especially for targeting therapy based on the small size effect.

Recent studies have shown that nanoparticle size has a non-trivial role in adhesion to biological cells, cellular uptake and further inhibition of tumor growth.<sup>21</sup> Generally, the size and shape of inorganic nanomaterials is related to the lattice rearrangement of the surface atoms to minimize the surface tension and Gibb's free energy.<sup>22–24</sup> The micro/nano-structural, or intrinsic, size governs a significant change to the bulk material's properties.<sup>25</sup> Therefore, some researchers have heavily focused on correlation studies between nanoparticle size and biological effect on siRNA-based therapeutics<sup>26</sup> or nanodelivery systems.<sup>27</sup> Owing to the challenging problem of synthetic techniques, the diameters of nanoplateforms for cancer therapy, which vary from 20 nm to 1.5 μm, are too large to be easily absorbed by the cells. It is known that the larger-sized nanoplateforms are not easily metabolized by the liver, spleen or kidneys. The agglomeration of larger nanoplateforms in the organs creates a huge potential risk of inducing cancer. To overcome this problem, it is essential to design and synthesize ultra-small nanoplateforms (~10 nm in diameter) with a surface modification that promotes biocompatibility, which will greatly increase the tumor-targeting retention of therapeutic agents and will allow them to be quickly cleared through glomerular filtration. Therefore, a targeted therapy nanoplateform based on the small size effect is urgently needed.

Herein, we developed a novel ultra-small and highly stable Fe<sub>3</sub>O<sub>4</sub>@P-NPO/PEG-Glc@Ce6 nanoplateform with diameters of 4, 8 and 13 nm for improving tumor-targeting efficiency and photodynamic therapeutic efficacy (Figure 1). As shown in Figure 1a, the versatile Fe<sub>3</sub>O<sub>4</sub>@P-NPO/PEG-Glc@Ce6 nanoplateform was composed of Fe<sub>3</sub>O<sub>4</sub>@P, NPO

dendrimer and PEGylated glucose (Glc). The photosensitizer Ce6 was loaded in the organic shell. The NPO dendrimer was utilized to improve both the loading efficiency of photosensitizer Ce6 and the biocompatibility of Fe<sub>3</sub>O<sub>4</sub>@P, and PEGylated Glc was used as the target molecule to enhance the efficiency of tumor targeting. In particular, Glc was introduced for enhancing cellular uptake of nanoparticles into malignant cells through specific cell recognition of cellular membranes.<sup>28,29</sup> We observed that the small size effect of Fe<sub>3</sub>O<sub>4</sub>@P-NPO/PEG-Glc@Ce6 nanoprobes has a key role in influencing the cellular uptake amounts, which were measured by a qualitative laser confocal microscope and the quantified detection technology of flow cytometry. Furthermore, we found that the Fe<sub>3</sub>O<sub>4</sub>@P-NPO/PEG-Glc@Ce6 nanoprobes can effectively prolong the residence time in the tumor region and reduce accumulation in the vital organs, including lung, liver and spleen 3 days post injection. We also successfully applied the Fe<sub>3</sub>O<sub>4</sub>@P-NPO/PEG-Glc@Ce6 nanoplateform in PDT in MGC-803 tumor-bearing mice. With the assistance of the visible red light irradiation, the nanoplateform can significantly inhibit the growth of tumors *in vivo*, and it exhibits excellent photodynamic therapeutic efficacy (Figure 1b).

## EXPERIMENTAL METHODS

### Materials

Iron(III) acetylacetonate (Fe(acac)<sub>3</sub>), oleylamine, oleic acid, benzyl ether, phenyl ether, chloroform, *N*-Boc-ethylenediamine, *N*-hydroxysuccinimide, chlorin e6 (Ce6) and 1-(3-dimethylaminopropyl)-3-ethylcarbodiimide hydrochloride were obtained from Aladdin reagent Co., Ltd. (Shanghai, China); glycidol, dioxane, NaH and NaHCO<sub>3</sub> were obtained from the Sinopharm Chemical Reagent Co., Ltd. (Shanghai, China); carboxyl-PEG<sub>10K</sub>-amine (HOOC-PEG<sub>10K</sub>-NH<sub>2</sub>, MW≈10 k) was obtained from Shanghai ZZbio Co., Ltd. (Shanghai, China); Hoechst 33342 1,2-hexadecanediol, glucose (4-aminophenylβ-D-glucopyranoside, Glc) and 3-[4,5-dimethylthiazol-2-yl]-2,5-diphenyltetrazolium bromide (MTT) were purchased from Sigma-Aldrich Chemical Co., Ltd. (St Louis, MO, USA). All chemical reagents were used as received, unless specified. MGC-803 cells were kindly supplied by the Chinese Academy of Science. Cell culture medium and other reagents were from Gibco

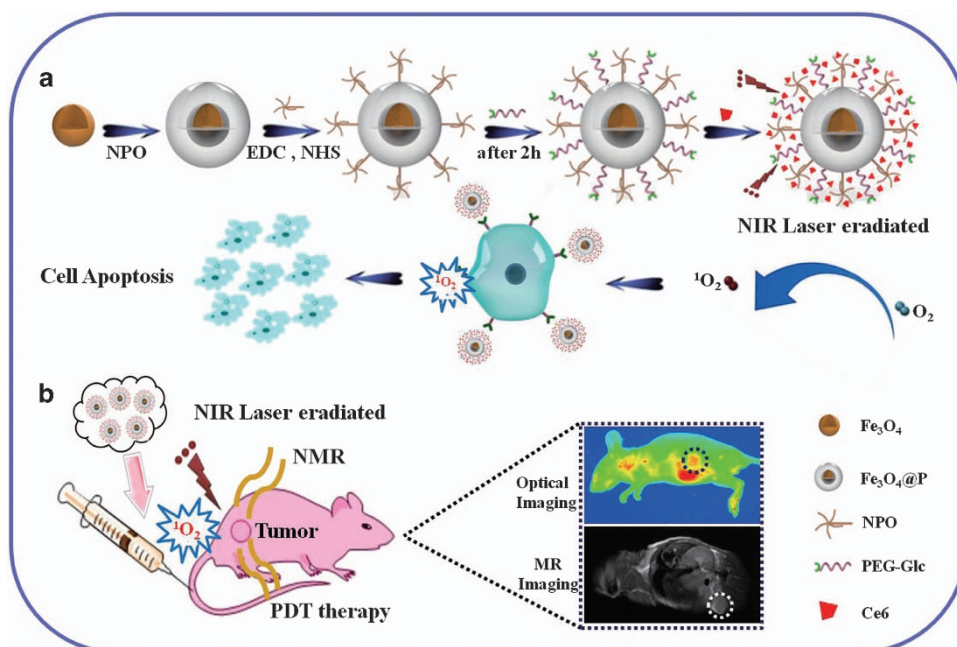


**Figure 1** Schematic of Fe<sub>3</sub>O<sub>4</sub>@P-NPO/PEG-Glc@Ce6 nanoprobes for *in vitro/vivo* dual modal diagnosis and treatment. (a) Formation of Fe<sub>3</sub>O<sub>4</sub>@P-NPO/PEG-Glc@Ce6 nanoprobes, (b) Photodynamic therapy in MGC-803 tumor-bearing mice.

(Shanghai, China). A Milli-Q water system (18.2 MΩ cm, Millipore Co., Bedford, MA, USA) provided the ultrapure water used in the experiments.

### Preparation of the Glc-targeting and Ce6-loaded nanoparticles

**Synthesis of monodisperse Fe<sub>3</sub>O<sub>4</sub> NPs (4 nm).** Monodisperse Fe<sub>3</sub>O<sub>4</sub> NPs with diameters of ~4 nm were produced by a reported procedure with slight modification.<sup>30</sup> Specifically, Fe(acac)<sub>3</sub> (2 mmol) and 1,2-hexadecanediol (10 mmol) were added to a three-neck flask with the addition of oleylamine (6 mmol), oleic acid (6 mmol) and 20 ml of phenyl ether. Under a N<sub>2</sub> environment and magnetic stirring, the temperature was gradually elevated to 200 °C for 0.5 h. Then the temperature was elevated to reflux (~265 °C) and aged for another 0.5 h. The reaction was stopped until the mixture was cooled to room temperature. After adding 30 ml ethanol, a brownish black product was precipitated via centrifugation at 3000 r.p.m. for 10 min. After removing the supernatant, the precipitate was dispersed in chloroform (20 ml), followed by adding dropwise oleic acid (5 μl) and oleylamine (5 μl). Afterwards, the brown products were precipitated and separated by centrifuge again (3000 r.p.m., 10 min). Finally, the products were redispersed in chloroform and kept at room temperature for further use.

**Synthesis of monodisperse Fe<sub>3</sub>O<sub>4</sub> NPs (8 nm).** Fe<sub>3</sub>O<sub>4</sub> NPs with diameters of ~8 nm were synthesized with the reported procedure with slight modification.<sup>30</sup> In brief, Fe(acac)<sub>3</sub> (2 mmol), benzyl ether (15 ml), oleic acid (6 mmol), oleylamine (6 mmol) and 1,2-hexadecanediol (10 mmol) were added in a three-neck flask and completely mixed. The solution was first slowly elevated to 200 °C and kept under N<sub>2</sub> protection with magnetic stirring for 2 h and then heated to 300 °C for aging for another 1 h. Finally, the reaction was complete, and the solution was cooled to room temperature. The washing step was followed by the procedure described above; afterwards, Fe<sub>3</sub>O<sub>4</sub> NPs (*d<sub>c</sub>* ~ 8 nm) were dissolved in chloroform.

**Synthesis of monodisperse Fe<sub>3</sub>O<sub>4</sub> NPs (13 nm).** Fe<sub>3</sub>O<sub>4</sub> NPs with diameters of ~13 nm were synthesized via a seed-mediated growth process.<sup>30,31</sup> The synthesized Fe<sub>3</sub>O<sub>4</sub> NPs (*d<sub>c</sub>* ~ 8 nm) were used as seeds and were grown up to Fe<sub>3</sub>O<sub>4</sub> NPs (*d<sub>c</sub>* ~ 13 nm). Typically, 1,2-hexadecanediol (10 mmol), Fe(acac)<sub>3</sub> (2 mmol) and 8 nm Fe<sub>3</sub>O<sub>4</sub> NP seeds (40 mg dispersed in 2 ml of chloroform) were injected into the three-neck flask followed dispersed by addition of oleylamine (2 mmol), benzyl ether (20 ml) and oleic acid (2 mmol). The obtained mixtures were elevated to 100 °C for 20 min to remove the chloroform. Afterwards, with N<sub>2</sub> flow and magnetic stirring, the temperature was increased to 200 °C for 1 h and then to 300 °C and held for another 0.5 h. During the synthesis, the color of the solution gradually changed from reddish brown to black. After terminating the reaction by the removal of the heating mantle, the black-colored product was washed with ethanol with the above-mentioned procedure and dispersed in chloroform.

**Synthesis of Fe<sub>3</sub>O<sub>4</sub> NPs encapsulated by amphiphilic polymer PMA (Fe<sub>3</sub>O<sub>4</sub>@P NPs).** Nonpolar Fe<sub>3</sub>O<sub>4</sub> NPs were transferred into an aqueous solution by coating with amphiphilic polymer using Parak's procedure.<sup>32</sup> During the polymer coating, with the addition of ~10 ml of chloroform, the hydrophobic Fe<sub>3</sub>O<sub>4</sub> NPs were mixed with the amphiphilic polymer in a 250-ml round-bottomed flask at a ratio of *R<sub>P/Area</sub>* = 1:300, where *R<sub>P/Area</sub>* is the ratio of the nanoparticle's specific surface area (nm<sup>2</sup>) to the polymer unit. Subsequently, the solvent in the round-bottom flask was evaporated by rotavap, and the solid film inside was dissolved by SBB 12 buffer (sodium borate buffer, 50 mM, pH = 12). Afterwards, the product was concentrated by centrifuge filter (Millipore, *M<sub>w</sub>* = 100 kDa) with centrifugation (3000 r.p.m., 10 min). Then, the remaining sample was precipitated and cleaned from excess free polymer via ultra-speed centrifuge (17 000 r.p.m., 1 h). The final washing step by ultra-speed centrifuge was performed three times to completely remove the free polymer. Finally, the cleaned PMA-coated Fe<sub>3</sub>O<sub>4</sub> NPs were dispersed in Milli-Q water.

**Synthesis of the NPO dendrimer.** The NPO dendrimer was prepared via the modified procedure.<sup>33</sup> The solution of *N*-Boc-ethylenediamine (0.999 mmol), glycidol (0.999 mmol) and 10 ml dioxane was added to a three-neck bottle at 90 °C and was stirred for 3 h. After the reaction, NaH (140 mg, 60% in mineral

oil) was added to the mixture and maintained for another 15 min. Glycidol (4.2 ml) in dioxane (10 ml) was added to the mixture dropwise and then stirred at 90 °C overnight. After the reaction, the organic layer was removed and the residue gel was dissolved in 10 ml water. The aqueous solution product was purified with a dialysis bag (MWCO 3k).

**Synthesis of the PEG-Glc.** The PEG-Glc was conjuncted using an amide bond. First, 20 nmol PEG was dissolved in 2 ml SBB9 using ultrasonic dispersion. Then, the carboxyl group on PEG was activated by adding 1-(3-dimethylaminopropyl)-3-ethylcarbodiimide hydrochloride and *N*-hydroxysuccinimide (100 μl, 0.25 mol l<sup>-1</sup>) for 20 min. After 5 mg Glc was added to the 2-ml tube, the mixture was left at 37 °C for 5 h on a shaking bed. The product solution was purified by an ultrafiltration device (Millipore, *M<sub>w</sub>* = 10 kDa) for 10 min at a centrifugal speed of 1.3 × 10<sup>4</sup> r.p.m. to 2 ml using ultrapure water, which was preserved at -20 °C.

**Preparation of the Fe<sub>3</sub>O<sub>4</sub>@P-NPO/PEG-Glc@Ce6 nanoparticles.** To activate the carboxyl group on different sizes of Fe<sub>3</sub>O<sub>4</sub>@P, 1-(3-dimethylaminopropyl)-3-ethylcarbodiimide hydrochloride and *N*-hydroxysuccinimide (200 μl, 0.03 mol l<sup>-1</sup>) were added for 20 min. Then, 300 μl 0.01 mol l<sup>-1</sup> PEG-Glc was coupled with activated Fe<sub>3</sub>O<sub>4</sub>@P-COOH. After 2 h, 10 μl NPO dendrimer was added to the mixture, which was then maintained at 37 °C for 5 h on a shaking bed. The product solution was purified by an ultrafiltration device (Millipore, *M<sub>w</sub>* = 100 kDa) for 20 min at a centrifugal speed of 3500 r.p.m. and was concentrated to 500 μl. Then, 5 mg ml<sup>-1</sup> 500 μl Ce6 dissolved in 0.01 M NaHCO<sub>3</sub> (pH 8.3) was mixed into the above concentrated solution. Finally, the unloaded Ce6 was removed using ultrafiltration (Millipore, *M<sub>w</sub>* = 100 kDa) for 20 min at a centrifugal speed of 3500 r.p.m., concentrated to 500 μl. Then, the characteristic absorbance of unloaded drug collected through ultrafiltration was determined. Based on the absorbance value at 404 nm and different concentrations of the standard curve, the unloaded drug content was obtained. The Ce6 loading capacity equation is shown as follows.

$$\text{Drug Loading Capacity (\%)} = \left( \frac{\text{the total added amount of drug} - \text{unloaded drug collected in ultrafiltration device}}{\text{the added amount of drug}} \right) \times 100$$

To remove bacteria, the colloidal solution of nanoprobes was sterilized by a 0.22 μm millipore express PES membrane filter unit. The release of Ce6 in the synthesized nanoprobe-13 nm in different phosphate-buffered saline (PBS) solutions (pH = 5.0, 7.4 and 10) was measured by UV-Vis spectrophotometry. Typically, 50 μl nanoprobe-13 nm was adjusted to 500 μl using PBS solution. After that, the mixture was fixed on a shaking bed at 35 °C. The 60 μl mixture was fixed at a point (0.5, 2, 5, 8, 12, 24 and 48 h) and washed using PBS and ultrafiltered water. The filtrate was collected for the determination of UV-Vis absorption values.

### Characterization

Transmission electron microscopy (TEM) was applied for the observation of synthesized nanoprobes (200 kV for nanoprobes and 80 kV for MGC-803-treated nanoprobes). The surface charge and the hydraulic diameter of the nanoprobes in ultrapure water were measured by a NICOMP 380ZLS zeta potential/particle size analyzer. UV-Vis absorption spectra were measured using a Varian Cary 50 UV-Vis spectrophotometer. Fourier transform infrared (FTIR) spectroscopy of Fe<sub>3</sub>O<sub>4</sub>@P-NPO/PEG-Glc@Ce6 nanoprobes was carried out by a Perkin Elmer spectrophotometer. Fluorescence spectra (PL) were determined through a Hitachi FL-4600 spectrofluorometer. Magnetic hysteresis loops of nanoprobes were obtained by a Physical Property Measurement System Ever Cool-II with 9 Tesla magnets (Quantum Design, San Diego, CA, USA) at 300 K. T<sub>2</sub> relaxation times of different sizes of nanoprobes were acquired on a 1.4 T Bruker Minispec Analyzer (MQ60). The concentrations of the samples were diluted with ultrapure water, shifted in sample tubes and immersed in a 37 °C circulating water bath pot to maintain a uniform temperature. After that, the *r*<sub>2</sub> value (mm<sup>-1</sup> s<sup>-1</sup>) corresponding to the three sizes of nanoprobes was obtained, which was the slope of the optimum straight line determined by fitting different T<sub>2</sub> values.

### Cell culture and MTT assay

MGC-803 gastric cancer cells were used in the current research. These were continuously incubated under 37 °C with 5% CO<sub>2</sub> in Dulbecco's Modified Eagle's medium medium supplemented with 100 U ml<sup>-1</sup> penicillin–streptomycin and 10% (vol/vol) FBS and were split at a ratio of 1:3 two times a week. The standard MTT assay was measured for evaluating the dark/phototoxicity of free Ce6 and the as-prepared NPs. In brief, MGC-803 cells at a density of 5000 cells per well were seeded in 96-well plates using 100 µl fresh Dulbecco's Modified Eagle's medium medium and cultured overnight for cell adherence and growth. The tumor cells were incubated with various concentrations of free Ce6, nanoprobe-4 nm, nanoprobe-8 nm or nanoprobe-13 nm for 1 day. After that, the growth medium was removed and the adherent cells were rinsed twice using PBS. When interacted with MGC-803 cells for another 4 h, MTT reagent (150 µl per well) was removed. Then, 150 µl of DMSO was added to each well to fully dissolve the solid formazan crystals for 10 min at room temperature. The optical density (OD) value per well was recorded by a Multiskan MK3 microplate reader (Thermo Scientific, Waltham, MA, USA) at 570 nm. The mean standard deviation (s.d.) of five parallel experiments for each concentration was calculated. The cytotoxicity was evaluated, and the formula was as follows:

$$\text{Cell viability} = \left( \frac{\text{OD value of the experimental group}}{\text{OD value of the control group}} \right) \times 100\%.$$

According to this formula, the cell activity of the control group was denoted as 100%.

### Cellular uptake assay

To investigate the cellular uptake assay qualitatively, confocal fluorescence imaging was carried out with a Leica TCS SP8 confocal laser scanning microscope. The tumor cells ( $7.0 \times 10^4$  cells per well) were seeded in a four-chamber glass-bottom dish to adhere overnight. Subsequently, the co-incubation interacted with three types of 5 nm nanoprobes and free Ce6 (Ce6 contained in 5 nm nanoprobe-13 nm equivalently) for 0.5, 4 and 12 h. After that, the adherent cells were rinsed using PBS and fixed for ~20 min by 4% paraformaldehyde at room temperature. Afterwards, the nuclei of the cells were stained using Hoechst 33342, which was excited at 405 nm and to give emission in the range of 440–460 nm. The emission of loaded Ce6 excited at 633 nm was tracked between 650 and 700 nm.

To further analyze cellular uptake quantitatively, flow cytometry measurements were taken using a BD FACSCalibur flow cytometer. MGC-803 cells ( $3.0 \times 10^4$  cells per well) were plated overnight in a 24-well dish. For another 0.5, 4 and 12 h, the fresh medium with concentrations corresponding to confocal imaging studies was added in each well. Finally, the adherent cells were rinsed twice using PBS, collected in 0.5 ml PBS and measured by flow cytometry. The fluorescence signal of MGC-803 cells was recorded by FL3 ( $\lambda_{\text{em}} = 650 - 700$  nm) channel.

### Cell viability and apoptosis assay

MGC-803 cells ( $3.0 \times 10^4$  cells per well) were plated overnight in a 24-well dish and then incubated in fresh medium with three types of 5 nm nanoprobes and free Ce6 (the Ce6 amounts were equal to 5 nm nanoprobe-13 nm) for 24 h. For another 20 min, the cells were treated with 20 µM DCFH-DA. After that, they were irradiated using a 633 nm laser at a power of 50 mW cm<sup>-2</sup> for 1 min per well or not. Thereafter, the cells were washed using sufficient PBS, were trypsinized and were resuspended in 500 µl PBS for flow cytometry measurements. The detected signal intensity was equivalent to the standard reactive oxygen species yield.

**Apoptosis assay.** According to the instruction manual of the Annexin V-FITC/PI apoptosis assay kit (Yeasen, Shanghai, China), the relative distribution of cellular injury, including cellular necrosis and apoptosis, was determined with or without a 633 nm laser (50 mW cm<sup>2</sup>) for 1 min. Specifically, MGC-803 cells ( $3.0 \times 10^4$  cells per well) were seeded in 24-well plates overnight before treatment with PBS, free Ce6 (Ce6 amounts equal to 5 nm nanoprobe-13 nm) and the nanoprobes (nanoprobe-4 nm, nanoprobe-8 nm and nanoprobe-13 nm all with 5 nm Fe<sub>3</sub>O<sub>4</sub> nuclei). After

24 h incubation, the tumor cells were rinsed two times using sufficient PBS and fresh medium was added. Then, the cells were irradiated using a 633 nm laser with 50 mW cm<sup>-2</sup> for 1 min per well or not. After incubation for another 24 h, the cells were washed twice with 4 °C pre-cooling PBS, harvested and resuspended in 100 µl of binding buffer. After 15 min co-incubation with 5 µl of PI and 2.5 µl of Annexin V in the dark at room temperature, 400 µl of 1 × binding buffer was evenly mixed in each sample tube. Then, a fluorescence signal was detected using different channels of the BD FACSCalibur (BD Biosciences, Mountain View, CA, USA). Finally, the obtained data were analyzed by FlowJo 7.6 software.

### Endocytosis of nanoprobe-4 nm, nanoprobe-8 nm and nanoprobe-13 nm

MGC-803 cells were incubated overnight in a six-well dish ( $10 \times 10^4$  cells per well). The fresh medium containing nanoprobe-4 nm, nanoprobe-8 nm and nanoprobe-13 nm (50 nm) was added and co-incubated for 24 h. After that, the MGC-803 cells were completely rinsed using PBS to eliminate the extracellular nanoparticles. Then, the cells were trypsinized, harvested (centrifuged at 1300 r.p.m. for 5 min) and fixed using 2.5% glutaraldehyde at 4 °C overnight. Then, the cells were sliced, stained and fixed on a copper network, per routine. Endocytosis and distribution of the three types of synthesized nanoprobes within cells were also carried out on an 80 KV B-TEM (Tecni G2 Spirit Biotwin, FEI). The MGC-803 cells without processing were detected as the control group (Supplementary Figure S12).

### *In vivo* magnetic resonance/fluorescence dual-modal imaging

The animal experiments were implemented in accordance with the Guidelines for Animal Care and Use Committee of Shanghai Jiao Tong University. Healthy female BALB/c-nude mice (6 weeks of age, body weight of  $20 \pm 3$  g) were obtained from Shanghai LAC Laboratory Animal Co. Ltd. and raised in the animal center. The *in vitro* tumor was knifed into small fragments of ~2 mm. After that, the nude mice were anesthetized, and an incision 3 mm in length was cut in the right flank skin of the mice. Subsequently, a patch of the fragments was quickly fixed in the slight incision. The incision was stitched. After 3 or 4 weeks, the subcutaneous xenografted tumor models of gastric cancer (GC) were formed. Each step was carried out under aseptic conditions.

The studies on magnetic resonance/fluorescence dual-modal imaging and biodistribution were performed when the tumor volume was ~150 mm<sup>3</sup>. Free Ce6 (the amounts of Ce6 were equal to 100 nm nanoprobe-13 nm) and the synthesized nanoprobes in PBS medium (100 nm) were intravenously injected into the gastric tumor-bearing mice via the tail. The fluorescent images *in vivo* ( $\lambda_{\text{ex}} = 630$  nm;  $\lambda_{\text{em}} = 700$  nm; exposure time, 30 s) at given recording intervals (blank, 0 h, 4 h, 8 h, 12 h, 24 h and 3 days) were carried with a Bruker *In Vivo* FPRO imaging system (Billerica, MA, USA). The fluorescent signals of *in vitro* major organs and tumors were also recorded on this imaging system in accordance with the parameters of the above-mentioned living image. The average fluorescence intensity of *in vitro* major organs and tumors was quantitatively calculated by Bruker Molecular Imaging Software Version 7.1.

All MR imaging studies *in vivo* were examined by a 3.0 T Siemens Magnetom Trio medical MR system (Shanghai Sixth People's Hospital Radiology Department of MRI, Shanghai, China). The parameters are: TR = 2600 ms, TE = 52 ms, slice thickness = 2 mm, FOV = 1 cm × 1 cm, matrix = 320 × 256, NEX = 2 and acquisition time 96 s. The tumor-bearing mice were anesthetized, put into a mating detection coil and scanned at recording intervals (blank, 0, 4, 8, 12 and 24 h) for three as-synthesized nanoprobes. The gray values were determined on a clinical MR system and processed using MR imaging software.

### *In vivo* small size and target molecule density synergistic efficiency

To assess the synergistic efficiency of both the small size and tumor targeting *in vivo*, the maximum and minimum diameters of the tumor were recorded by Vernier caliper every 3 days, and then the tumor volume was calculated. We compared five groups using tumor-bearing mice upon laser irradiation with nanoprobe-4 nm (with Glc; doses were equivalent to the moles of Fe<sub>3</sub>O<sub>4</sub> core NPs in nanoprobe-13 nm), nanoprobe-8 nm (with Glc; doses equivalent to moles of Fe<sub>3</sub>O<sub>4</sub> core NPs in nanoprobe-13 nm), nanoprobe-13 nm (with Glc; doses were equivalent to 5 mg kg<sup>-1</sup> Ce6), free Ce6 (5 mg kg<sup>-1</sup>), and a control

group (100  $\mu$ l PBS), in which a 633 nm laser with 50 mW cm<sup>-2</sup> was used for 30 min after 8 and 24 h post injection. The corresponding optical photograph and tumor size of each tumor-bearing mouse were acquired every 3 days up to 18 days. At day 18, the main organs (for example, brain, spleen, kidney, heart, lung and liver) of these mice were harvested and then drenched in 4% paraformaldehyde at 4 °C overnight. After that, the collected organ tissues were sliced, fixed on a slide, and stained using hematoxylin and eosin in accordance with conventional procedures. Finally, the morphological features and pathological changes of these tissues were microscopically examined in detail.

## RESULTS

### Preparation and characterization of NPO dendrimer

The synthetic route of dendritic polyglycerol (NPO) dendrimer is shown in Supplementary Figure S1. A series of nuclear magnetic resonance (NMR) spectra, such as <sup>1</sup>H (Supplementary Figure S2) and <sup>13</sup>C (Supplementary Figure S3), were analyzed to verify the structure and relative molecular weight of the NPO. The quantitative analysis of the <sup>1</sup>H NMR spectra indicates that the number-average ( $M_n$ ) molecular weight is 15 860 g mol<sup>-1</sup>. The <sup>1</sup>H NMR spectra of NPO show the characteristic proton signals of -CH<sub>2</sub>O- and -CHO- units of NPO in the range of 3.4–4.0 p.p.m., and the amino group of NPO as a reactive end group is observed at approximately 2.5 p.p.m., which overlaps with the solvent peak. FTIR data (Supplementary Figure S4) were evaluated to further support the <sup>1</sup>H NMR spectral measurements. The wide absorption band at 3406 cm<sup>-1</sup> suggested overlapping multiple alcoholic hydroxyl stretching vibrations.<sup>34</sup> The peaks at 1112 and 2879 cm<sup>-1</sup> were attributed to the C–O–C and C–H stretch vibrations on the NPO chain, respectively.<sup>35</sup> The characteristic peak at 1639 cm<sup>-1</sup> confirmed the formation of C–NH<sub>2</sub>, which corresponds to the asymmetric variable angle vibration of the N–H bond in the primary amine, known as the amide I absorption band.<sup>36</sup>

### Synthesis and characterization of Fe<sub>3</sub>O<sub>4</sub> NPs

The three types of MNPs with different sizes were synthesized by adapting the solvothermal parameters. Figures 2a, d and g show typical TEM images of the as-synthesized Fe<sub>3</sub>O<sub>4</sub> NPs. The three types of MNPs have a mean diameter of 3.26 ± 0.68 nm (Figure 2c), 7.96 ± 0.92 nm (Figure 2f) and 12.97 ± 1.29 nm (Figure 2i) based on statistical analysis of 300 nanoparticles. High-resolution TEM (HR-TEM) images of representative NPs (Figures 2b,e and h) clearly show that the lattice fringes (~2.6 Å) across the whole NPs match with a spinel Fe<sub>3</sub>O<sub>4</sub> structure.

### Synthesis and characterization of Fe<sub>3</sub>O<sub>4</sub>@P-NPO/PEG-Glc@Ce6 NPs

The as-synthesized Fe<sub>3</sub>O<sub>4</sub>@P NPs were subsequently modified using NPO hyperbranched polyimide and Glc by 1-(3-dimethylaminopropyl)-3-ethylcarbodiimide hydrochloride and *N*-hydroxysuccinimide coupling, and then Ce6 molecules were loaded. To graft the targeted Glc molecule onto the surfaces of Fe<sub>3</sub>O<sub>4</sub> NPs, we first modified Glc using COOH-PEG<sub>10K</sub>-NH<sub>2</sub> through carboxyl–amino group coupling. To prove the presence of PEG-functionalized Glc, the characteristic peak of the benzene ring in <sup>1</sup>H NMR spectroscopy was clearly recorded at ~6–7 p.p.m. (Supplementary Figure S5b), which is similar to the value of pure Glc (curve b in Supplementary Figure S5b). FTIR analysis further confirmed the successful synthesis of the PEG-Glc. The characteristic peak at 1641 cm<sup>-1</sup> confirmed the presence of tumor-targeted Glc, which corresponds to amide I peaks (Supplementary Figure S5a). The TEM images of the three types of synthesized Fe<sub>3</sub>O<sub>4</sub>@P-NPO/PEG-Glc@Ce6 NPs are shown in Figures 3a–c. To verify the successful surface modification of the

Fe<sub>3</sub>O<sub>4</sub> NPs, zeta potential measurements were performed (Figure 3d). The Fe<sub>3</sub>O<sub>4</sub> NPs (~4, 8 and 13 nm in diameter) encapsulated by the amphiphilic polymer (containing moieties rich in carboxyl groups) have negative potentials of -35.42, -29.33 and -30.29 mV, respectively. The surface potentials of the Fe<sub>3</sub>O<sub>4</sub> NPs modified using NPO and PEGylated Glc showed a significant increase and were measured to be -12.66, -10.66 and -5.46 mV, respectively.

The hydrodynamic sizes of the Fe<sub>3</sub>O<sub>4</sub>@P NPs before and after surface modification were also determined using dynamic light scattering, as shown in Figure 3e. It can be observed that the hydrodynamic sizes of the three types of Fe<sub>3</sub>O<sub>4</sub>@P NPs were 17, 25.7 and 31.2 nm. The corresponding Fe<sub>3</sub>O<sub>4</sub>@P-NPO/PEG-Glc@Ce6 NPs were 13.8, 28.9 and 39 nm, respectively. Compared with the initial Fe<sub>3</sub>O<sub>4</sub> NPs, the increase of the hydrodynamic size of Fe<sub>3</sub>O<sub>4</sub>@P-NPO/PEG-Glc@Ce6 nanoprobcs was attributed to the surface modification process of the initial Fe<sub>3</sub>O<sub>4</sub> NPs. Excitingly, the hydrodynamic size of the nanoprobe-4 nm, nanoprobe-8 nm and nanoprobe-13 nm in PBS solution changed very little after storage for 1 month (Supplementary Figure S6d), indicating that the three types of Fe<sub>3</sub>O<sub>4</sub> nanoparticles have excellent colloidal stability in PBS solution. To further confirm their excellent colloidal stability, the three types of synthesized Fe<sub>3</sub>O<sub>4</sub> nanoparticles were further tested by dispersing them into water, PBS and cell culture medium over 1 month. The results showed that no precipitation occurs for the three types of Fe<sub>3</sub>O<sub>4</sub> nanoprobcs (Supplementary Figures S10a and S11). Furthermore, the three types of Fe<sub>3</sub>O<sub>4</sub> nanoprobcs had excellent red fluorescence (Supplementary Figure S10b). Those results show that these three types of Fe<sub>3</sub>O<sub>4</sub> nanoprobcs can be applied in *in vivo* diagnosis and treatment.

To confirm the successful synthesis of the three nanoprobcs, FTIR spectra and UV-Vis absorption were measured. It was found that the components in the Fe<sub>3</sub>O<sub>4</sub>@P-NPO/PEG-Glc@Ce6 nanoprobcs, such as NPO and PEG-Glc, were anchored on the surface of Fe<sub>3</sub>O<sub>4</sub>@P (Supplementary Figure S7). The characteristic absorption peak at 1112 cm<sup>-1</sup> was assigned to the C–O–C bond of NPO,<sup>35</sup> and this peak has a shift to lower frequency, indicating the presence of amide bonding between Fe<sub>3</sub>O<sub>4</sub>@P and NPO. In addition, the absorption peak at 280 nm in the UV-Vis spectrum indicated the presence of glucose, which is consistent with the characteristic absorption peak of the phenyl group from pure glucose. The variations in the characteristic peak from FTIR spectra illustrated that the Glc was successfully bonded with Fe<sub>3</sub>O<sub>4</sub> NPs through the formation of an amide bond between glucose and PEG. By comparison with free Ce6 (641 nm), the UV-Vis spectroscopy also indicated that there was a significant bathochromic shift in the region of the Ce6 Q(I) band of nanoprobe-4 nm (665 nm), nanoprobe-8 nm (673 nm) and nanoprobe-13 nm (660 nm), which is a typical characteristic of Ce6 in different chemical environments.<sup>8</sup> The results indicated that free Ce6 was successfully encapsulated by the NPO. Interestingly, the characteristic peak intensity of the three types of nanoprobcs (700 nm) in the region of the Ce6 Q (II) band was markedly higher than that of free Ce6. This was ascribed to the formation of a conjugated double bond structure, leading to a decrease of  $\pi$  electron transition energy when free Ce6 was wrapped tightly in the shell of NPO. The variation of nanoprobe-4 nm is the most evident (Supplementary Figure S6a), which can be attributed to the small size effect.

To evaluate the chemical properties of the synthesized nanoprobcs, the PL spectra, saturation magnetization value ( $M_s$ ) and the T2 relaxation rate were analyzed. Generally, the near-IR fluorescence intensities of the three types of nanoprobcs were partially reduced by self-quenching, as they aggregate easily through  $\pi$ – $\pi$  conjugated bond stacking<sup>37</sup> and generate resonance energy transfer.<sup>38</sup> However, the

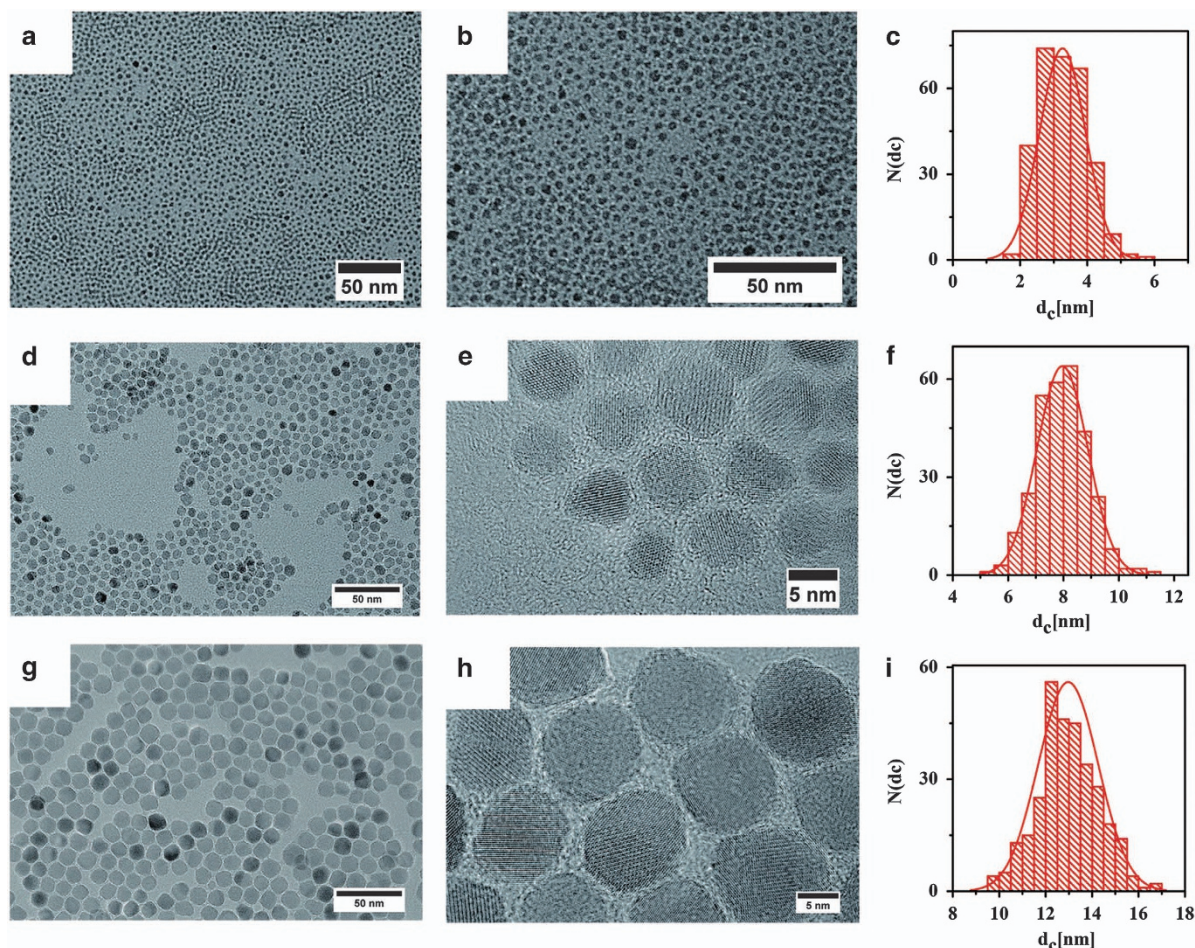


**Figure 2** Characterization of the Fe<sub>3</sub>O<sub>4</sub> NPs. (a, d, g) TEM of the as-synthesized Fe<sub>3</sub>O<sub>4</sub> NPs. (b, e, h) HR-TEM images of some representative Fe<sub>3</sub>O<sub>4</sub> NPs. (c, f, i) Size distribution of the diameter of the Fe<sub>3</sub>O<sub>4</sub> NPs obtained from TEM measurements using Image J software (red histogram). The distribution is fitted using a normal distribution function (red curve).

emission peak of Ce6 was observed at 660 nm, suggesting their potential for near-infrared fluorescence imaging (Supplementary Figure S6b). It is noteworthy that the fluorescence intensity of nanoprobe-8 nm was the lowest; this was attributed to the high surface activity. The field-dependent magnetization curve revealed that both the Fe<sub>3</sub>O<sub>4</sub> NPs and the Fe<sub>3</sub>O<sub>4</sub>@P-NPO/PEG-Glc@Ce6 nanoprobes exhibited superparamagnetic properties at room temperature, which was an important factor for the T2 contrast agents (Supplementary Figure S8).<sup>39</sup>

By fitting the function between the relaxation rate (1/T<sub>2</sub>) and the Fe concentration, the r<sub>2</sub> of the Fe<sub>3</sub>O<sub>4</sub> NPs (4 nm, 8 nm, 13 nm) were calculated to be 6.00, 54.03 and 156.02 mm<sup>-1</sup> s<sup>-1</sup>, respectively (Supplementary Figure S6c). The r<sub>2</sub> of the Fe<sub>3</sub>O<sub>4</sub>@P-NPO/PEG-Glc@Ce6 nanoprobes (4, 8 and 13 nm) were calculated to be 4.97, 44.31 and 127.71 mm<sup>-1</sup> s<sup>-1</sup>, respectively. Obviously, the T<sub>2</sub> relaxivity of Fe<sub>3</sub>O<sub>4</sub> NPs was slightly higher than that of the corresponding nanoprobes. The presence of NPO and PEGylated Glc moieties on the surface of nanoprobes might have a slight shielding effect on the coating layers, thereby hindering the accessibility between Fe<sub>3</sub>O<sub>4</sub> core NPs.<sup>40</sup> It is interesting to note that nanoprobe-8 nm and nanoprobe-13 nm had a higher r<sub>2</sub> value than nanoprobe-4 nm, which was crucial for the T<sub>2</sub>-weight negative contrast agents of the MR imaging. In other words, the MR signal value significantly decreased with the increase in NP concentration.

To evaluate the small size effect, we measured three types of Fe<sub>3</sub>O<sub>4</sub>@P-NPO/PEG-Glc@Ce6 nanoprobes at the same Fe concentration gradient (Supplementary Figure S9). The fluorescence intensity of nanoprobe-13 nm was highest, at a concentration of 0.56 mM [Fe], with the signal decreasing with further increases in concentration. The fluorescence intensity of nanoprobe-4 nm and nanoprobe-8 nm reach the highest level at a concentration of 0.0175 and 0.28 mM [Fe], respectively. The higher intensity was attributed to the large surface activity of the smaller particles. The smaller diameter was prone to resonance energy transfer within the scope of the ultra-small particle based on the small size effect.

The loading capacities of Ce6 in the three types of Fe<sub>3</sub>O<sub>4</sub>@P-NPO/PEG-Glc@Ce6 nanoprobes were 5.09, 8.2 and 9.22%. As expected, the larger nuclear size can bond more NPO and PEGylated Glc, leading to loading much more Ce6. To evaluate the releasing behavior of Ce6 from the synthesized nanoprobe-13 nm in different PBS solutions (pH=5.0, 7.4 and 10), the UV-Vis absorption was measured (Supplementary Figure S12). The results show that nanoprobe-13 nm exhibited excellent stability in the pH=5 PBS solution. In addition, the variation trend of the absorption values maintained a nearly constant value in the PBS solutions of pH=7.4 and 10, implying that nanoprobe-13 nm was highly stable and not easily affected by the medium.

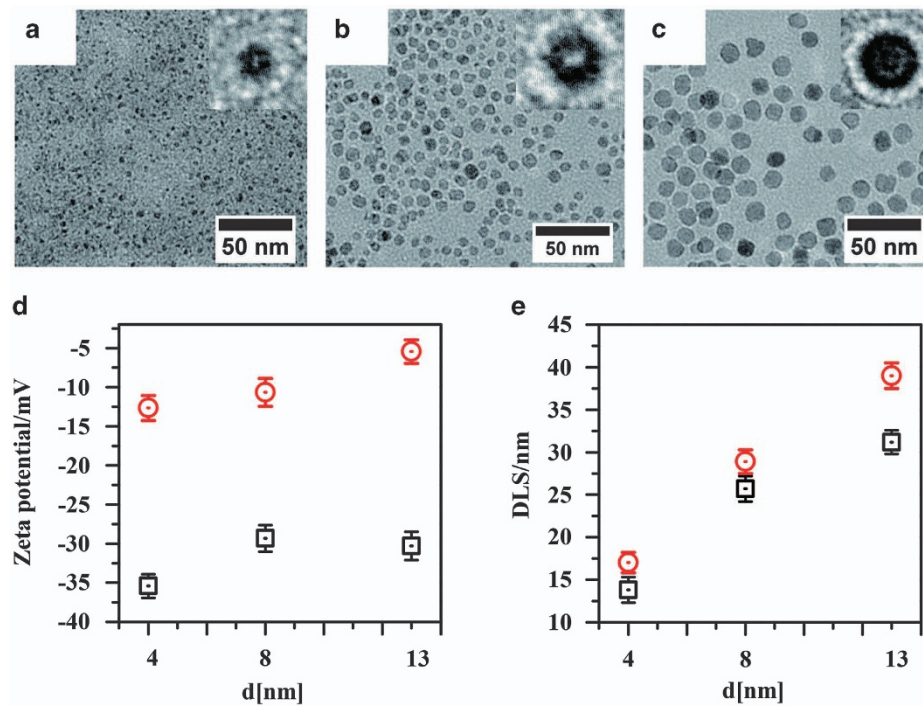


**Figure 3** Characteristics of the Fe<sub>3</sub>O<sub>4</sub>@P-NPO/PEG-Glc@Ce6 NPs. (a-c) TEM of the as-synthesized Fe<sub>3</sub>O<sub>4</sub>@P-NPO/PEG-Glc@Ce6 NPs. (d) Zeta potential of intermediate Fe<sub>3</sub>O<sub>4</sub>@P and the as-synthesized Fe<sub>3</sub>O<sub>4</sub>@P-NPO/PEG-Glc@Ce6 NPs. (e) The hydrodynamic diameter of intermediate Fe<sub>3</sub>O<sub>4</sub>@P and as-synthesized Fe<sub>3</sub>O<sub>4</sub>@P-NPO/PEG-Glc@Ce6 NPs.

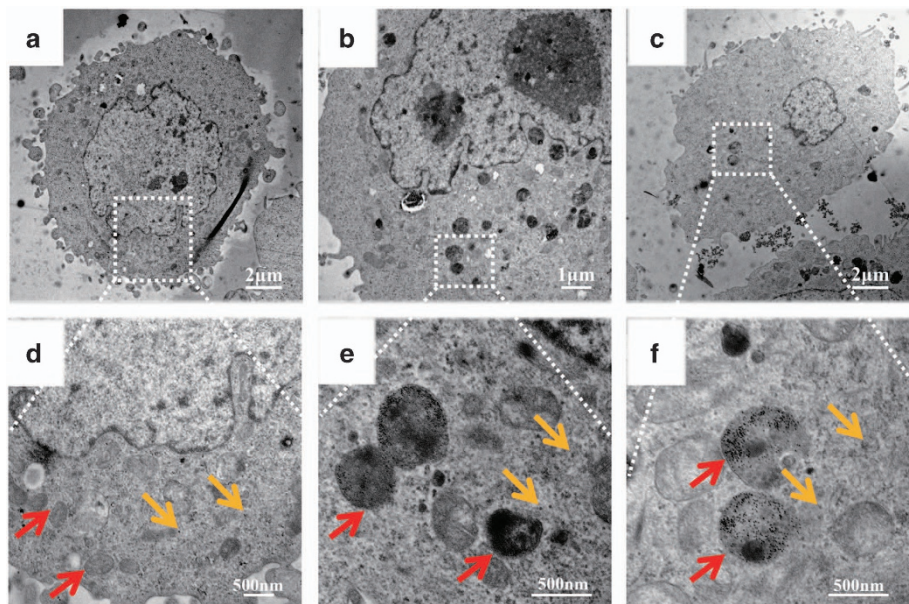


**Figure 4** Representative TEM images of MGC-803 cells. Ultrastructures of MGC-803 cells after incubation with nanoprobe-4 nm (a, d), nanoprobe-8 nm (b, e) and nanoprobe-13 nm (c, f) for 24 h, respectively. Red arrows and yellow arrows represent the location of nanoprobes. Note that the red arrows represent the nanoprobes located in the lysosome, the yellow arrows represent nanoprobes dispersions being exocytosed by the MGC-803 cells.

**Cellular uptake and intracellular distribution based on size and target molecule density synergistic efficiency**

The cellular uptake of the three types of Fe<sub>3</sub>O<sub>4</sub>@P-NPO/PEG-Glc@Ce6 nanoprob involves phagocytosis, a process of internalizing materials by engulfing them with the cell membrane to display the

intracellular distribution of the three types of nanoprob. TEM images were used to confirm the internalization of these nanoprob. Figure 4 shows that the nanoprobes were distributed in lysosomes and endosomes with little aggregation compared with the control group (Supplementary Figure S13). The reason for the lack of aggregation

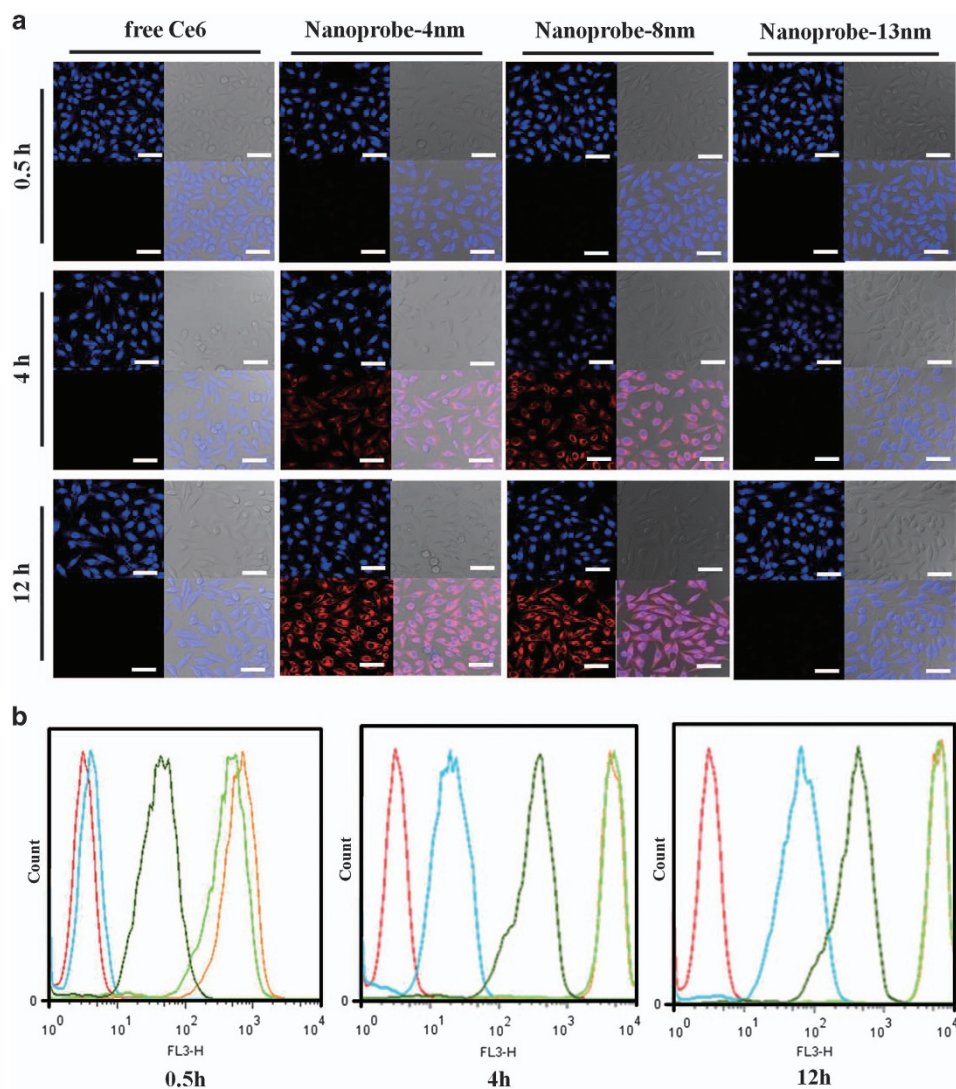


**Figure 5** Cellular uptake and localization in MGC-803 cells. (a) The qualitative laser confocal images of MGC-803 cells incubated with nanoprobe-4 nm, nanoprobe-8 nm, nanoprobe-13 nm and free Ce6 for 0.5, 4 and 12 h. (b) The quantitative flow cytometry graphs of cellular uptake for 0.5, 4 and 12 h. The scale bar is 100  $\mu$ m.

can be attributed to the fact that the NPO chains and PEGylated Glc on the surface of the nanoprobes consume the original carboxyl of Fe<sub>3</sub>O<sub>4</sub> NPs and increase the surface potential of the nanoprobes.<sup>41</sup> In addition, MGC-803 cells have high Glc expression, meaning that the intratumoral distribution of nanoprobes can be further improved.<sup>29</sup> Interestingly, we observed that the nanoprobes internalized by cells were wrapped in a double membrane and were well-dispersed in the cells. This behavior can be assigned to the corrosion behavior in the extremely acid lysosomes, resulting in the exfoliation of the organic protective layer on the nanoprobes.<sup>42–44</sup>

To assess the small size effect of the synthesized Fe<sub>3</sub>O<sub>4</sub>@P-NPO/PEG-Glc@Ce6 nanoprobes on cells, confocal images were obtained and flow cytometry was carried out. It is widely accepted that particle size has a key role in targeting cell interaction and endocytosis.<sup>45</sup> The three types of Fe<sub>3</sub>O<sub>4</sub>@P-NPO/PEG-Glc@Ce6 nanoprobes and free Ce6 (equivalent to Ce6 in nanoprobe-13 nm) were incubated with MGC-803 cells for different times ( $t=0.5, 4$  and 12 h). A confocal laser scanning microscope was used for the qualitative analysis of the cellular uptake of the three types of

nanoprobes, and the results are shown in Figure 5a. Flow cytometry was also used to quantitatively analyze the ingestion of the nanoprobes, and the results are shown in Figure 5b. Owing to the targeting effect of Glc molecule, nanoprobe-13 nm was ingested more readily than free Ce6 after 12 h. The average value of the fluorescence intensity of the nanoprobes at 12 h was ~ sixfold higher compared with the control group (free Ce6). However, it is noteworthy that nanoprobe-4 nm and nanoprobe-8 nm were clearly ingested considerably more than nanoprobe-13 nm and free Ce6, due to the small size effect of ultra-small particles. When the MGC-803 cells were incubated with nanoprobe-4 nm for 0.5 h, the average value of the fluorescence intensity was approximately 155-fold higher compared with the control group (free Ce6). After successive incubation (4 h), the average fluorescence intensity values were ~228-fold higher. These results can be attributed to the synergistic efficiency of both the size effect and tumor-targeted molecule recognition. In addition, the increase in the zeta potential of the particle surfaces was beneficial for interaction with the negatively charged outer membrane of the cells.<sup>41</sup>



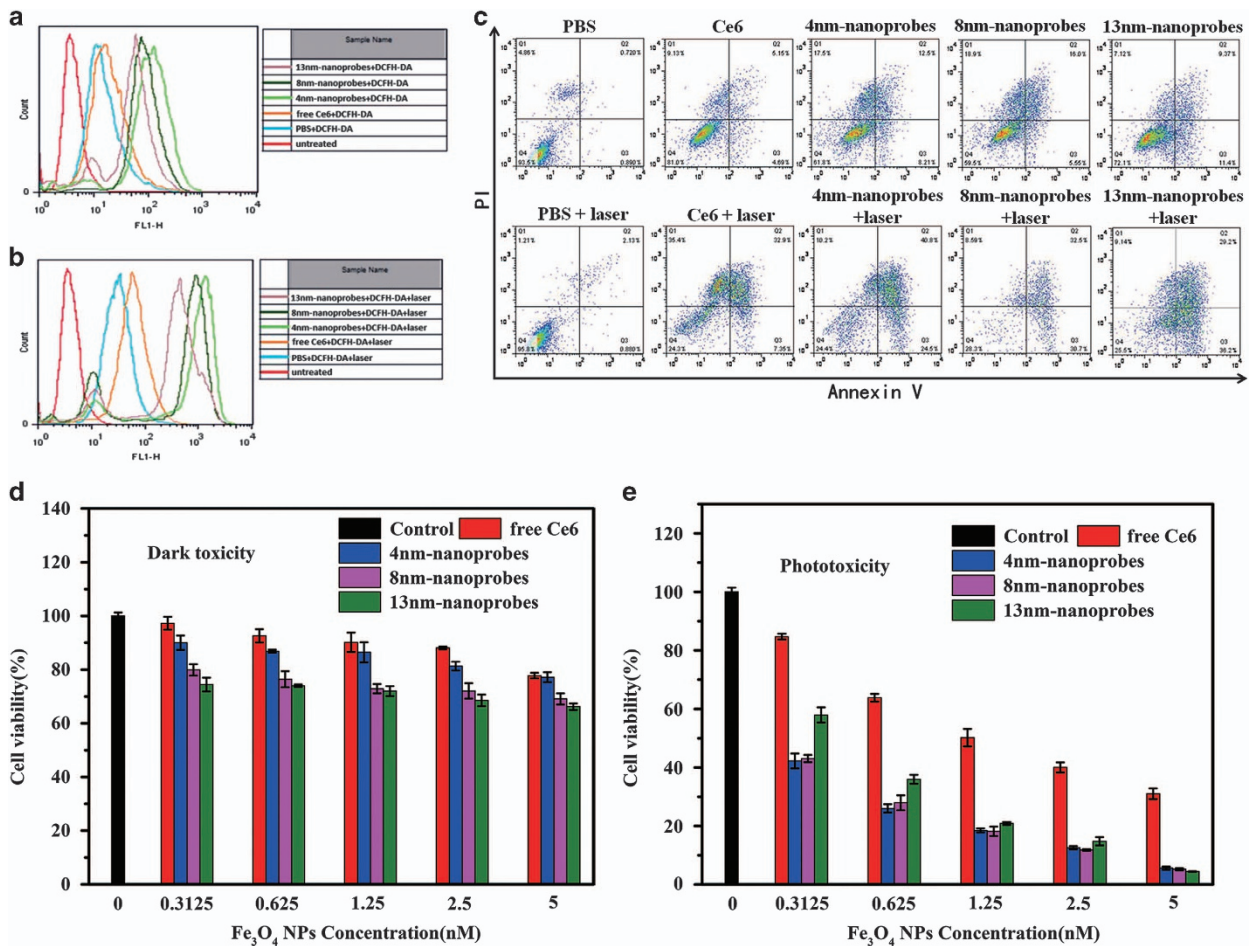


**Figure 6** *In vitro* cellular toxicity of the synthesized nanoprobe. (a, b) Flow cytometry detection of ROS generation using DCFH-DA with or without 633 nm laser irradiation. (c) Cell apoptosis after incubated 24 h between MGC-803 and three nanoprobe with or without 633 nm laser irradiation, respectively. (d, e) Dark/phototoxicity of free Ce6, three kinds of nanoprobe toward MGC-803 cells for 24 h of incubation, estimated by MTT assay.

### *In vitro* cell toxicity

It is known that the formation of singlet oxygen resulting from exposure to a laser could result in membrane disruption and subsequent cell death.<sup>8</sup> To confirm the phototoxicity of the three types of Fe<sub>3</sub>O<sub>4</sub>@P-NPO/PEG-Glc@Ce6 nanoprobe, the standard DCFH-DA staining protocol was carried out to evaluate their ability to generate intracellular singlet oxygen. As shown in Figure 6a, without the laser, the synthesized nanoprobe produced singlet oxygen with a similar ability, slightly more than free Ce6. Upon exposure to the laser, the amount of singlet oxygen generated by the nanoprobe was much higher than that of free Ce6 (Figure 6b). Obviously, the singlet oxygen generated by nanoprobe-4 nm and nanoprobe-8 nm was higher than that of nanoprobe-13 nm, which is consistent with the above results. An apoptosis assay of three types of Fe<sub>3</sub>O<sub>4</sub>@P-NPO/PEG-Glc@Ce6 with and without laser irradiation was performed for further quantitative investigation of the phototoxicity efficacy for the three types of nanoprobe. The flow cytometry measurement after Annexin V-FITC and propidium iodide double staining followed the standard manual procedure. Figure 6c shows that the laser itself cannot affect the cell activity. After treatment using the nanoprobe in the dark, the proportion of cell apoptosis was slightly higher than that of free Ce6-treated cells, which is consistent with the results of dark toxicity using MTT assay. However, the ratios of cell apoptosis in

MGC-803 co-incubated with nanoprobe-4 nm, nanoprobe-8 nm and nanoprobe-13 nm after 24 h with laser irradiation were markedly improved to 65.3%, 63.2% and 65.4%, respectively, compared with those treated with free Ce6 under the same condition (40.25%).

Generally, the generation of singlet oxygen by nanoprobe makes it feasible to use the particles as an effective nanoprobe for PDT. The biocompatibility of nanoprobe is also an important aspect for *in vivo* application. The potential cytotoxicity of the nanoprobe was evaluated through the standard MTT assay. Figure 6d shows that cell activity rarely decreased with the increase in nanoprobe concentration, and no obvious cytotoxicity was observed at doses up to 5 nM. The excellent biocompatibility without laser irradiation was attributed to the encapsulation of NPO and PEGylated Glc as a modified layer. In addition, phototoxicity was evaluated by measuring cell activity with the same serial concentration of dark toxicity under the 633 He-Ne laser irradiation (50 mW cm<sup>-2</sup>) for 1 min. Figure 6e shows that the cell viability decreased rapidly with the increase of nanoprobe concentration under laser irradiation. Compared with free Ce6, the three types of synthesized nanoprobe all had a good effect when used in PDT. This was attributed to the improved cellular uptake of the three types of nanoprobe and the effective production of ROS under laser irradiation, as demonstrated above.

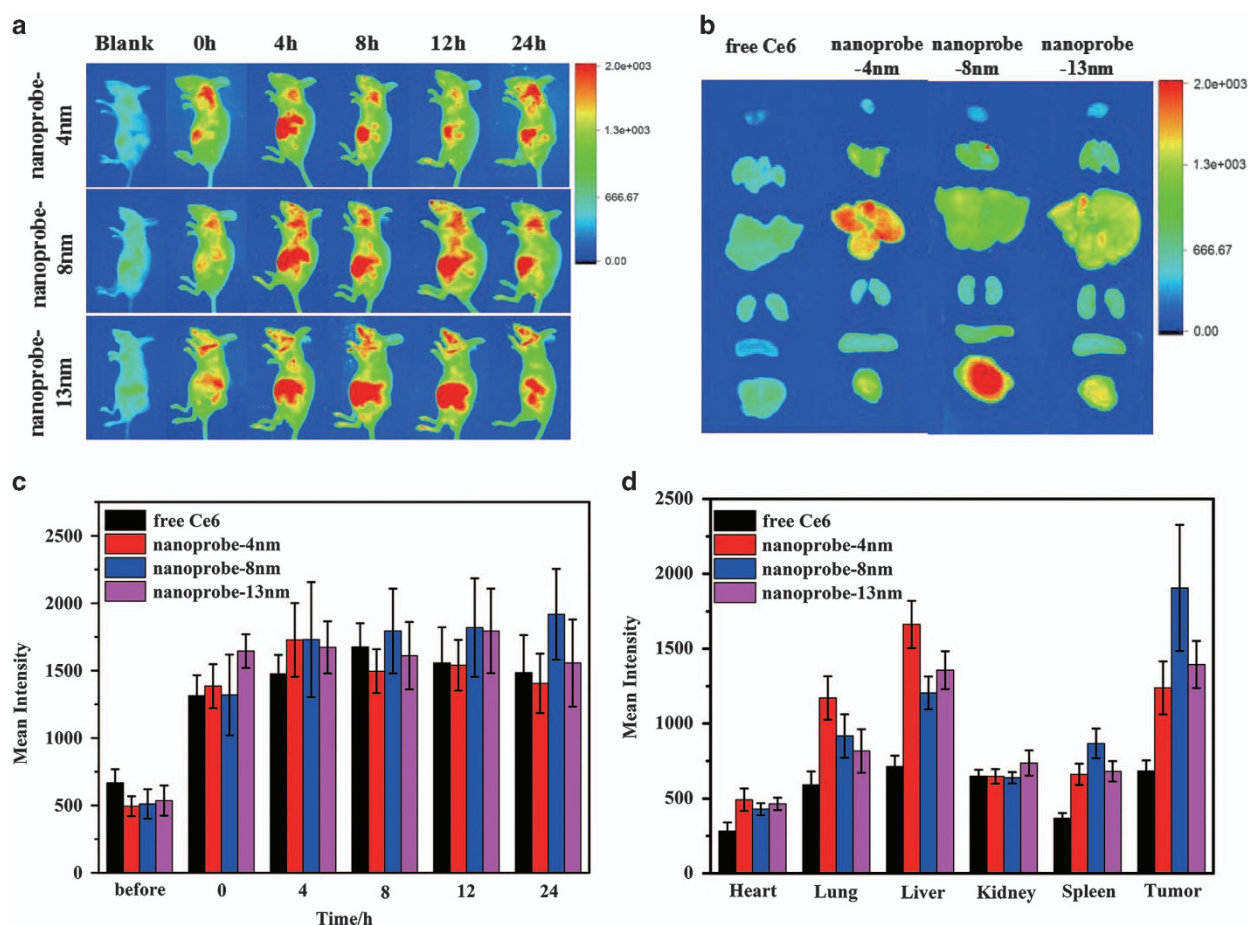


**Figure 7** The fluorescence images and biodistribution of three kinds of nanoprobes *in vivo* and organs and tumors *in vitro*. (a) The *in vivo* fluorescence imaging of mice after intravenous injection of nanoprobe-4 nm, nanoprobe-8 nm and nanoprobe-13 nm by real-time observation for 24 h. (b) The *in vitro* fluorescence images of major organs and tumors of mice after 24 h intravenous injection of free Ce6 and three kinds of nanoprobes. (c) The quantitative analysis of average fluorescence signals in the tumor sites of tumor-bearing mice after intravenous injection of these nanoprobes by real-time observation for 24 h. (d) The quantitative analysis of average fluorescence signals of major organs and tumors *in vitro* of mice after intravenous injection of three kinds of nanoprobes and free Ce6 over a period of 24 h. The parallel data are exhibited as mean  $\pm$  s.d. ( $n=5$ ).

### Tumor-targeting evaluation of the Fe<sub>3</sub>O<sub>4</sub>@P-NPO/PEG-Glc@Ce6 NPs based on the small size effect

According to the above results, we believe that the tumor therapy efficacies based on the small size effect can be demonstrated by *in vivo* treatment of tumor-bearing mice using different sizes of nanoprobes. To illustrate this idea, the tumor-bearing mice were intravenously injected with 100 nM nanoprobes in PBS solution, and the real-time distribution of the nanoprobes was monitored using a noninvasive optical imaging technique in real-time to evaluate their tumor-targeting capabilities. From Supplementary Figure S14, the fluorescence signal of free Ce6 mainly appeared in the liver. The fluorescence intensity has almost no accumulation in the tumor site of tumor-bearing mice treated with free Ce6. Furthermore, the fluorescence signal in the whole body of the mouse decreased rapidly after 24 h post injection, where it nearly had no fluorescent signal. The results suggest that free Ce6 is a small molecule which was easily metabolized by the mice. However, the three types of synthesized Fe<sub>3</sub>O<sub>4</sub>@P-NPO/PEG-Glc@Ce6 nanoprobes exhibited a relatively long tumor retention time and high tumor-targeting efficiency. Figure 7a shows that the fluorescence signal in the whole body of the mouse could be maintained for over 24 h. In addition, the fluorescence intensity in

the tumor site of the nanoprobe-treated mice was remarkably constant. The results show that the synthesized Fe<sub>3</sub>O<sub>4</sub>@P-NPO/PEG-Glc@Ce6 nanoprobes can prolong circulation time and tumor-targeting ability. It was found that the fluorescence intensity in the tumor region of the mice treated with nanoprobe-4 nm reached a maximum value at 4 h post injection, which is different from the mice treated with free Ce6. Nanoprobe-8 nm and nanoprobe-13 nm reached the strongest fluorescent signal at 24 and 12 h post injection, respectively. The different tumor retention times were also attributed to the small size effect of the nanoprobes. To quantitatively evaluate tumor-targeting efficacy based on the small size effect, a fluorescence intensity quantification assay was carried out. The results indicate that the average fluorescence intensity of the nanoprobe-4 nm at the tumor tissue was  $\sim$ 1.07-fold higher than that of free Ce6 at 24 h post injection, and the average fluorescence intensity of Ce6 in nanoprobe-8 nm and nanoprobe-13 nm in the tumor tissue was approximately 1.44-fold and 1.15-fold higher than free Ce6, as shown in Figure 7c. To confirm the tumor-targeting efficiency *in vivo*, the mice were euthanized at 24 h post injection in the control and experimental groups, respectively. The organs (spleen, liver, heart, kidneys and lungs) and tumors were acquired and imaged by *in vitro* fluorescence

imaging. Consistent with the *in vivo* observation, the excellent tumor-targeted efficiency based on the small size effect of nanoprobres was confirmed again. Figures 7b and d show that the near-infrared signals of mice treated with nanoprobe-8 nm and nanoprobe-13 nm were largely located in tumor, and a few nanoprobres were distributed in the lungs, liver and spleen. We also noted a strong Ce6 fluorescence intensity signal of mice treated with nanoprobe-4 nm was observed in the liver.

To estimate the metabolic pathways, the mice were killed at 3 days post injection for the experiment group. Fluorescence images *in vitro* of the organs and the tumor were taken. Supplementary Figure S15a shows that the fluorescence intensity signal of mice treated with nanoprobe-4 nm was largely located in the tumor, and minor residues were found in normal tissues (spleen, liver and lung). The time-dependent images demonstrate that the three nanoprobres had different metabolic pathways because of the different diameters. Interestingly, we found that the fluorescence intensity signal of mice treated with nanoprobe-4 nm and nanoprobe-13 nm 3 days post injection was almost as high as that at 24 h post injection. The fluorescence intensity of mice treated with nanoprobe-8 nm 3 days post-injection was slightly lower than that at 24 h post injection. The mean fluorescence intensity of Ce6 in the tumor and main organ tissues was also quantified (Supplementary Figure S15b). This result indicates that the three nanoprobres can all efficiently load the Ce6 to the tumor, prolong their residence time at the tumor site, and accumulate less in the normal organs (including lung, liver and spleen).

To validate the initial tumor-targeting efficacy based on both targeted molecules and the small size effect of nanoprobres, MR imaging was used to colocalize the tumor site. It is known that superparamagnetic Fe<sub>3</sub>O<sub>4</sub> nanoprobres are excellent T2-weighted contrast agents for MR images. In our experiment, MR images were investigated before and after injection. Figure 8a shows that all the three types of Fe<sub>3</sub>O<sub>4</sub>@P-NPO/PEG-Glc@Ce6 nanoprobres can provide in MR contrast enhancement at MGC-803 tumors. The average gray values of the T2-weighted MR images of nanoprobe-8 nm and nanoprobe-13 nm in the tumor were quantified, as shown in Figure 8b. The variation trends of gray values for nanoprobe-8 nm and nanoprobe-13 nm were consistent with the results obtained by the fluorescence images. However, the gray value of T2-weighted MR images in the tumor site of the mice treated with nanoprobe-4 nm reached a maximum value at 8 h post injection, which shows little difference from the results obtained by the fluorescence images. This is attributed to the low magnetic saturation intensity of nanoprobe-4 nm, leading to an inaccurate MR image. Because the nanoprobe-4 nm could be accumulated at the tumor site, it is not a problem for fluorescence imaging-guided cancer therapy. Based on the above results, the application of nanoprobe-8 nm and nanoprobe-13 nm for fluorescence/MR imaging-guided cancer therapy is a promising future application.

#### ***In vivo* photodynamic therapeutic efficacy of Fe<sub>3</sub>O<sub>4</sub>@P-NPO/PEG-Glc@Ce6 NPs**

To study the photodynamic therapeutic efficacy of the Fe<sub>3</sub>O<sub>4</sub>@P-NPO/PEG-Glc@Ce6 nanoprobres (nanoprobe-4 nm, nanoprobe-8 nm and nanoprobe-13 nm), the maximum and minimum tumor diameters of MGC-803 tumor-bearing mice after various treatment were measured using Vernier caliper for 18 days (Figure 9a). After 8 and 24 h post injection, the tumor sites of the blank group (PBS), the control group (free Ce6) and the experimental group (nanoprobe-4 nm, nanoprobe-8 nm and nanoprobe-13 nm) were exposed under a 633 nm laser

(50 mW cm<sup>2</sup>) for 30 min. Figure 9b shows that the growth tumor of the nanoprobe-13 nm/laser-treated mice was dramatically inhibited by 77% compared with that of the PBS/laser-treated mice. The results demonstrate the effectiveness of nanoprobe-13 nm for fluorescence/MR imaging-guided cancer PDT. As for the control group, the free Ce6-treated mice under the laser only showed 39% tumor growth inhibition. The improved performance of the nanoprobres was attributed to specific tumor-targeted capabilities and long-term accumulation in the tumor site. Furthermore, the inhibition ratio of tumor growth of the nanoprobe-4 nm/laser-treated mice and the nanoprobe-8 nm/laser-treated mice showed an excellent value of 66 and 71% at 18 days post treatment, respectively. The results demonstrate that our synthesized nanoprobe-4 nm and nanoprobe-8 nm can effectively inhibit tumor growth as promising nanoprobres.

The potential toxic side effects *in vivo* of the three types of Fe<sub>3</sub>O<sub>4</sub>@P-NPO/PEG-Glc@Ce6 nanoprobres were also investigated. The change in body weight of tumor-bearing mice after PDT was a visual factor to evaluate the side effects of the three types of nanoprobres. Figure 9d shows that no evident weight changes of the mice were recorded in any of the groups. To further confirm the potential *in vivo* toxicity of the three types of nanoprobres, the above-mentioned mice after 18 days of treatment were killed, and the main organs (heart, kidneys, spleen, brain, lungs and liver) were harvested. Then, these collected tissues were sliced and stained with hematoxylin and eosin in accordance with the standard manual protocol. The optical microscopy in Figure 9c shows that no apparent lesions or other abnormal signs were observed for the mice treated with the three nanoprobres compared with the mice from the blank group. Clearly, no evident side effects *in vivo* were observed after the PDT. The lower retention of the nanoprobres in normal tissue (including lung, liver and spleen) was also confirmed.

#### **DISCUSSION**

Compared with the reported chemotherapy strategies over recent years, our proposed photodynamic tumor treatment method using Fe<sub>3</sub>O<sub>4</sub>@P-NPO/PEG-Glc@Ce6 nanoprobres may resolve several critical challenges in cancer PDT. This is in contrast with the conventional pH-dependent nanoparticles, whose therapeutic efficacies may be significantly affected owing to increased surface hydrophobicity and therefore aggregation of free Ce6 by neutralization of carboxyl groups at lower pH. A pH-independent strategy utilized NPO dendrimers as a shielding layer for the Ce6 in the microenvironment of tumor tissue. This may inhibit Ce6 aggregation or even decompose partially pre-existing Ce6 aggregates, thus maintaining the monomer morphology of the photosensitizer. Previous research has shown that Ce6 mainly exists in the monomeric form in the peripheral blood<sup>46</sup> and upon cellular uptake<sup>47</sup> in the normal biological system. The aggregation of the photosensitizing agent can severely affect the PDT efficacy,<sup>48</sup> and the pharmacokinetic properties also lead to lower efficiency for traditional strategies. In contrast, our designed Fe<sub>3</sub>O<sub>4</sub>@P-NPO/PEG-Glc@Ce6 nanoprobres can enhance the hydrophilic properties of hydrophobic mono- and diethyl ethers of Ce6 through the interaction of Ce6 with NPO dendrimers. Furthermore, our strategy revealed that the Fe<sub>3</sub>O<sub>4</sub>@P-NPO/PEG-Glc@Ce6 nanoprobres lead to more targeted accumulation and longer retention in the tumor tissue than Ce6 alone. In addition, the Fe<sub>3</sub>O<sub>4</sub>@P-NPO/PEG-Glc@Ce6 nanoprobres have a faster elimination rate from normal tissues because of the synergistic effects between the small size effect and the structure of nanoprobres. Based on the ability of nanoparticles to passively target tumors through the enhanced permeability and retention effect,<sup>49</sup> the delivery of Ce6 upon intravenous injection in the tail involves inner

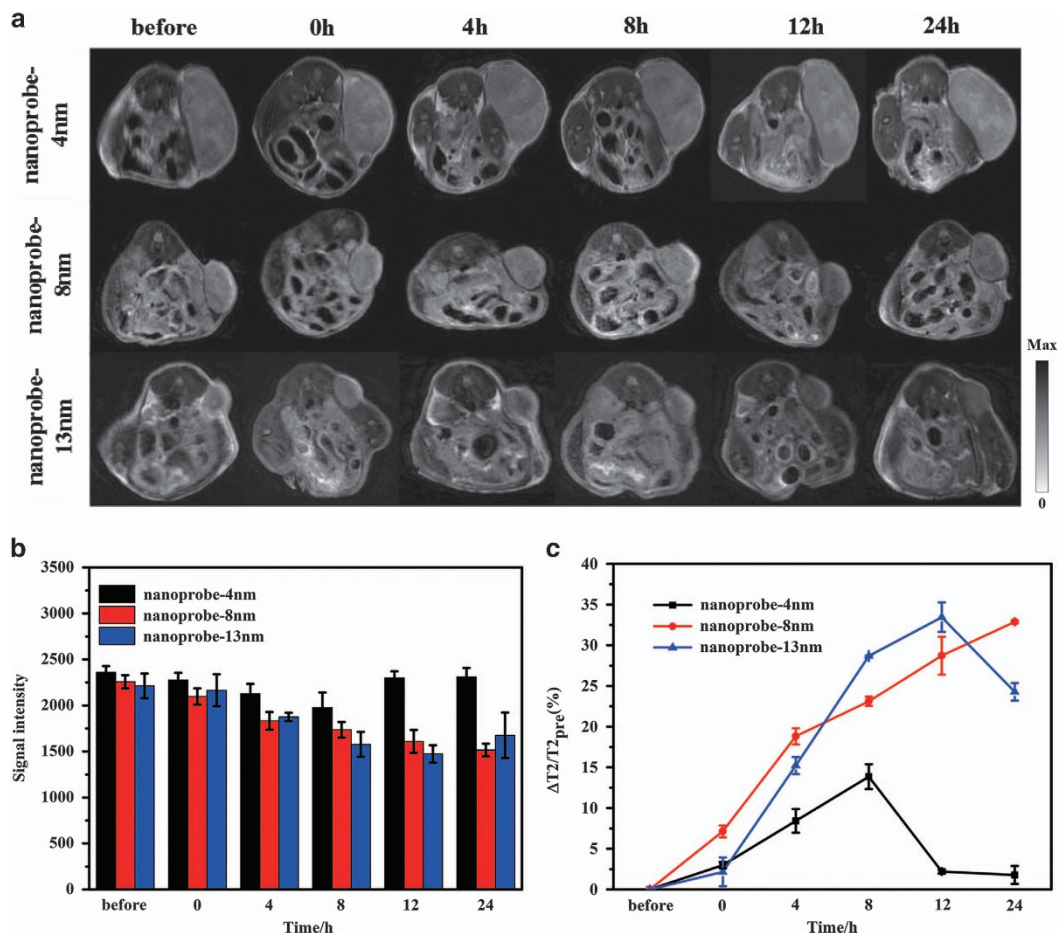


**Figure 8** *In vivo* MRI. (a) MR imaging of MGC-803 tumor-bearing mice after tail intravenous injection of nanoprobe-4 nm, nanoprobe-8 nm and nanoprobe-13 nm by real-time observation for 24 h. (b) The quantitative analysis of average signal intensity in the tumor site after intravenous injection of these nanoprobes by real-time observation for 24 h. (c) The growth curve of average signal intensity ( $\Delta T2/T2_{pre}$ ) after intravenous injection of nanoprobe-4 nm, nanoprobe-8 nm and nanoprobe-13 nm by real-time observation for 24 h. The parallel data are exhibited as mean  $\pm$  s.d. ( $n=5$ ).

carrier molecules in biological systems, in particular, human serum albumin. In case of fast redistribution, we speculate that a multifold Fe<sub>3</sub>O<sub>4</sub>@P-NPO/PEG-Glc@Ce6-human serum albumin was formed in the bloodstream. As a result, these hypothetical multicomponent complexes may have far more opportunities to reach the tumor region and reside there for a longer time owing to the enhanced permeability and retention effect.<sup>50</sup> Simultaneously, the specific surface characterization and the activity of the Fe<sub>3</sub>O<sub>4</sub>@P-NPO/PEG-Glc@Ce6 nanoplatform can be improved with the decrease of particle size. The number of binding sites and the binding force of Fe<sub>3</sub>O<sub>4</sub>@P-NPO/PEG-Glc@Ce6-human serum albumin may be improved due to the small size effect of nanoprobes. It is recognized that NPO dendrimers could act as a proton acceptor (through terminal hydroxyl). Hydrogen bonds could be produced in the acid tumor microenvironment, which would be beneficial for the retention of the nanoplatform at the tumor site for subsequent PDT efficacy.

The size-dependent property of cellular uptake was analyzed via the entry mechanism of the Fe<sub>3</sub>O<sub>4</sub>@P-NPO/PEG-Glc@Ce6 nanoprobes. It has been suggested that the major pathway of nanoprobes entering cells is endocytosis, including clathrin-mediated endocytosis, caveolae-mediated endocytosis and macropinocytosis, which is based on energy dependence.<sup>51,52</sup> Er-Wei Song *et al.*<sup>26</sup> reported that the smaller 40 nm nanoparticles can be internalized by malignant cells through caveolae

and clathrin-dependent endocytosis, but not macropinocytosis. As for the design of our Fe<sub>3</sub>O<sub>4</sub>@P-NPO/PEG-Glc@Ce6 nanoprobes, the adoptive diameters of the Fe<sub>3</sub>O<sub>4</sub> cores were <40 nm. Thus, the entry mechanism of these Fe<sub>3</sub>O<sub>4</sub>@P-NPO/PEG-Glc@Ce6 nanoprobes was also via the above two pathways. However, the cellular uptake of these nanoprobes was distinguished according to an energy-dependent mechanism. In other words, the smaller nanoprobes may more easily bind with tumor cells in accordance with the small size effect. Furthermore, different-sized nanoprobes may result in the extension of apoptosis. For the above-mentioned nanoprobes, the percentage of early apoptotic cells after treatment with nanoprobe-4 nm, nanoprobe-8 nm and nanoprobe-13 nm was 40.8%, 32.5% and 29.2%, respectively. In contrast, that of the fully apoptotic cells was 24.5%, 30.7% and 36.2%, respectively. Based on these results, it can be concluded that an increase in nanoprobe size can enhance the overall apoptotic cells by endocytosis owing to an increased amount of Ce6 into cells in a given time. The percentage of early apoptotic cells was improved with a decrease in nanoprobe size. This was attributed to the small size effect enhancing the cellular uptake of nanoprobes at the same time.

Compared with the *in vitro* results, the size effect of the Fe<sub>3</sub>O<sub>4</sub>@P-NPO/PEG-Glc@Ce6 NPs on antitumor efficacies presented some differences. The increase of the Fe<sub>3</sub>O<sub>4</sub>@P-NPO/PEG-Glc@Ce6

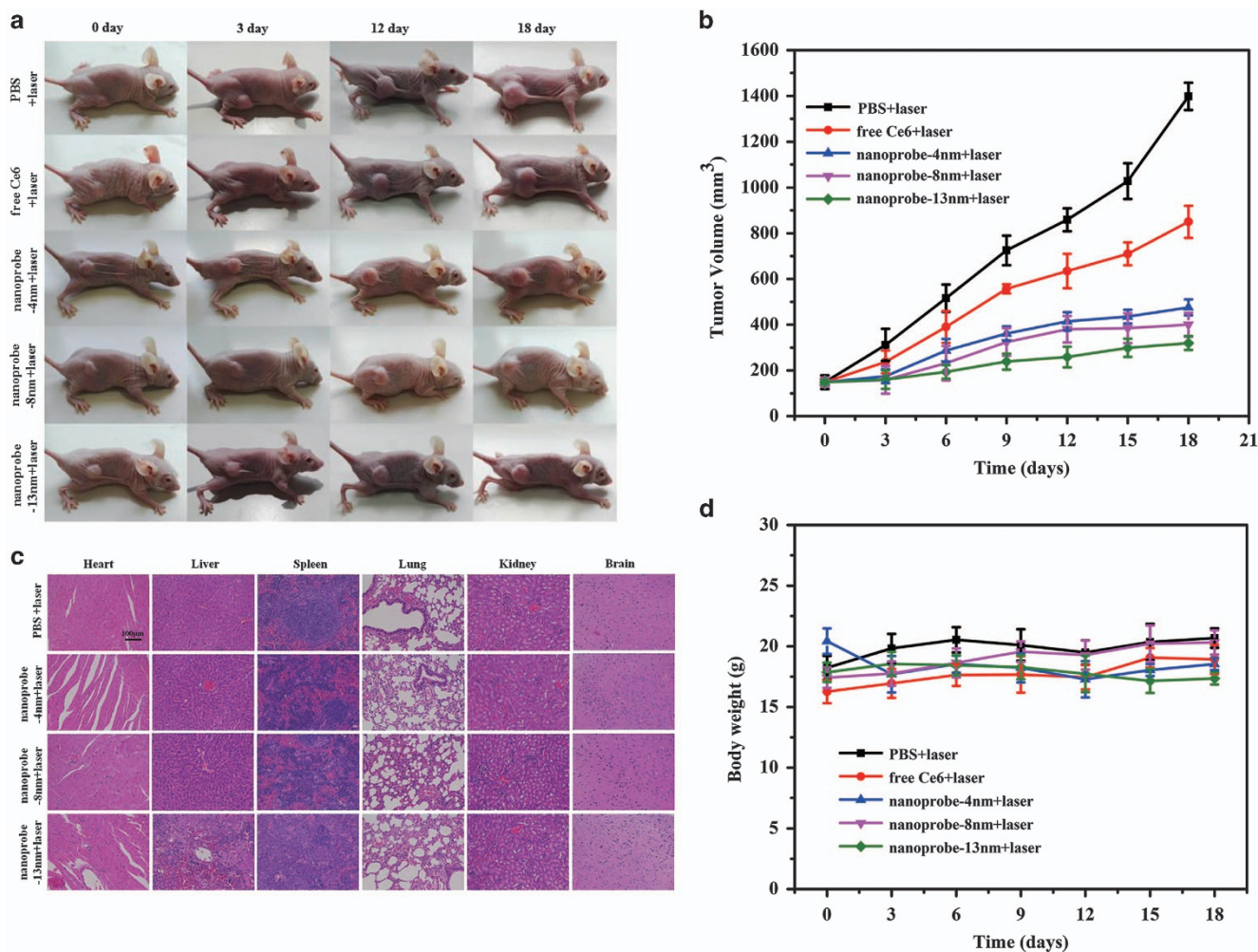


**Figure 9** *In vivo* photodynamic therapeutic efficacy and toxic side effect of nanoprobes. (a) The optical photograph of tumor-bearing mice after intravenous injection of nanoprobes (4 nm, 8 nm and 13 nm) in five groups pre- and post treatment. The solid tumor sites of each model mice in different groups were irradiated using 633 nm laser (50 mW cm<sup>-2</sup>) for 30 min after 8 and 24 h post injection. (b) The tumor growth curve of tumor-bearing mice after treatment for 18 days. (c) The slices of the organs and H&E staining containing brain, lung, liver, kidney, heart and spleen of tumor-bearing mice treated with PBS and three kinds of nanoprobes under the laser irradiation after day 18. The scale bar is 100  $\mu$ m. (d) The curves in body weight of mice after different treatment over a period of 18 days. The parallel data are exhibited as the mean  $\pm$  s.d. ( $n=5$ ).

nanoprobe size inhibited the rapid growth of tumors, which is attributed to the higher loading of drugs in larger nanoprobes. The inhibition rate of tumor growth in the largest 13 nm-nanoprobe/laser-treated mice was merely an 11% increase over that of the smallest 4 nm-nanoprobe, which demonstrated the photodynamic therapeutic efficiency of the Fe<sub>3</sub>O<sub>4</sub>@P-NPO/PEG-Glc@Ce6 NPs based on the size-dependent effect. However, the targeting efficiency of target molecules may be different *in vitro* and *in vivo*. The *in vitro* results indicated that a decrease in the Fe<sub>3</sub>O<sub>4</sub>@P-NPO/PEG-Glc@Ce6 nanoprobe size leads to an increase in targeted efficiency because of the enhanced cellular uptake. However, among the investigated nanoplateforms, the largest 13 nm-nanoprobe exhibited the best photodynamic therapeutic efficiency for tumors, which may be partly due to the increase in the steric hindrance for the smallest nanoprobes via the formation of multifold Fe<sub>3</sub>O<sub>4</sub>@P-NPO/PEG-Glc@Ce6-human serum albumin in the bloodstream, which is consistent with the above-mentioned hypothesis. The *in vivo* experiments showed that there may be a certain balance between the ultra-small size of

nanocarriers and the number of target molecules for internalization, retention and overall antitumor efficacy in the complex biological system.

Our results have demonstrated that the size of the nanoplateform has a crucial role in adhesion to and interaction with the tissue cells. In particular, the introduction of bio-adhesive materials such as poly(ethylene glycol) and artificial dendrimers (monomer structure of NPO is similar to poly(ethylene glycol)) can greatly enhance their adhesion to and internalization into the intestinal cells as well as the inhibiting capacity of combination with the multi-drug resistance pump proteins.<sup>21</sup> After injection into mice via the tail vein, the possible mechanism for the <50-nm nanoparticles may be paracellular passage. That is, nanoparticles between intestinal epithelial cells pass through the barriers by the kneading method.<sup>53</sup> Moreover, <20-nm nanoprobes can significantly promote transport in both the tumor stroma and the vessel walls. They can then be cleared through glomerular filtration,<sup>54</sup> which ideally reduces the side effects on organs.

## CONCLUSIONS

In summary, we have successfully developed novel Fe<sub>3</sub>O<sub>4</sub>@P-NPO/PEG-Glc@Ce6 nanoplatfoms for PDT that have low cytotoxicity and excellent biocompatibility. By conjugating target molecule glucose with Fe<sub>3</sub>O<sub>4</sub>@P-NPO, the internalization ability for MGC-803 cells *in vitro* and the photodynamic effect of Fe<sub>3</sub>O<sub>4</sub>@P-NPO/PEG-Glc@Ce6 *in vivo* were both improved. The nanoplatfoms gave a more accurate diagnosis before cancer treatment using the colocalization of fluorescence images and MR images. Most importantly, with the help of the qualitative laser confocal microscope and quantified detection technology of flow cytometry, the size of the nanocarriers, that is, the small size effect, also had a critical role in determining the cellular uptake besides the target molecule. In particular, the photosensitizer Ce6 via the as-synthesized nanoplatfom Fe<sub>3</sub>O<sub>4</sub>@P-NPO/PEG-Glc@Ce6 was found to prolong the residence time in the tumor region, and lead to less accumulation in the normal tissue (including lung, liver and spleen) after 24 h or 3 days post injection. Based on these improvements, the strategy exhibited excellent photodynamic therapeutic efficacy by inhibiting the growth of tumors in mice under 633 nm laser irradiation with a relatively lower power. Compared with previously reported inorganic-based photodynamic agents, which are usually characterized by a complicated design and difficulties in controlling the sizes of nanoparticles, the combination of ultra-small Fe<sub>3</sub>O<sub>4</sub> NPs with dendrimers in our strategy will significantly help in the design of further research, and it holds great promise for cancer therapy in the future.

## CONFLICT OF INTEREST

The authors declare no conflict of interest.

## ACKNOWLEDGEMENTS

We are grateful for the financial support from the National Natural Science Foundation of China (No. 81671737, 81225010 and 91634108), the 863 High-Tech project of China (2014AA020701) and the 973 Project (2015CB931802). The support of the Australian Research Council Discovery Program (DP130101714) is gratefully acknowledged.

*Author contributions:* GG and DC conceived and designed the research project. TY, QZ, HW, YS, QH, PH and WQ performed the experiments, data acquisition and characterization. JGS participated in the mechanism analysis. All the authors contributed to the data analysis and the writing of this manuscript, and all authors reviewed the manuscript and gave their approval to the final version of the manuscript.

- Huebsch, N. & Mooney, D. J. Inspiration and application in the evolution of biomaterials. *Nature* **462**, 426–432 (2009).
- Wang, C., Xu, H., Liang, C., Liu, Y. M., Li, Z. W., Yang, G. B., Cheng, L., Li, Y. G. & Liu, Z. Iron Oxide@Polypyrrole nanoparticles as a multifunctional drug carrier for remotely controlled cancer therapy with synergistic antitumor effect. *ACS Nano* **7**, 6782–6795 (2013).
- Garg, T., Jain, N. K., Rath, G. & Goyal, A. K. Nanotechnology-based photodynamic therapy: concepts, advances and perspectives. *Crit. Rev. Ther. Drug Carrier Syst.* **32**, 389–439 (2015).
- Zhang, C., Zhao, K., Bu, W. B., Ni, D. L., Liu, Y. Y., Feng, J. W. & Shi, J. L. Marriage of scintillator and semiconductor for synchronous radiotherapy and deep photodynamic therapy with diminished oxygen dependence. *Angew. Chem. Int. Ed.* **54**, 1770–1774 (2015).
- Castano, A. P., Demidova, T. N. & Hamblin, M. R. Mechanisms in photodynamic therapy: part two-cellular signaling, cell metabolism and modes of cell death. *Photodiagnosis Photodyn. Ther.* **2**, 1–23 (2005).
- James, M. C. J. Photodynamic therapy: a review. *Drugs Aging* **1**, 49–68 (1999).
- Huang, P., Lin, J., Wang, S. J., Zhou, Z. J., Li, Z. M., Wang, Z., Zhang, C. L., Yue, X. Y., Niu, G., Yang, M., Cui, D. X. & Chen, X. Y. Photosensitizer-conjugated silica-coated gold nanoclusters for fluorescence imaging-guided photodynamic therapy. *Biomaterials* **34**, 4643–4654 (2013).
- Zhang, C. L., Li, C., Liu, Y. L., Zhang, J. P., Bao, C. C., Liang, S. J., Wang, Q., Yang, Y., Fu, H. L., Wang, K. & Cui, D. X. Gold nanoclusters-based nanoprobes for simultaneous fluorescence imaging and targeted photodynamic therapy with superior penetration and retention behavior in tumors. *Adv. Funct. Mater.* **25**, 1314–1325 (2015).
- Huang, P., Lin, J., Wang, X. S., Wang, Z., Zhang, C. L., He, M., Wang, K., Chen, F., Li, Z. M., Shen, G. X., Cui, D. X. & Chen, X. Y. Light-triggered theranostics based on photosensitizer-conjugated carbon dots for simultaneous enhanced-fluorescence imaging and photodynamic therapy. *Adv. Mater.* **24**, 5104–5110 (2012).
- Ge, J. C., Lan, M. H., Zhou, B. J., Liu, W. M., Guo, L., Wang, H., Jia, Q. Y., Niu, G. L., Huang, X., Zhou, H. Y., Meng, X. M., Wang, P. F., Lee, C. S., Zhang, W. J. & Han, X. D. A graphene quantum dot photodynamic therapy agent with high singlet oxygen generation. *Nat. Commun.* **5**, 4596 (2014).
- Yaghini, E., Seifalian, A. M. & MacRobert, A. J. Quantum dots and their potential biomedical applications in photosensitization for photodynamic therapy. *Nanomedicine* **3**, 353–363 (2009).
- Guan, M. R., Dong, H., Ge, J. C., Chen, D. Q., Sun, L. D., Li, S. M., Wang, C. R., Yan, C. H., Wang, P. F. & Shu, C. Y. Multifunctional upconversion-nanoparticles-trimethylpyridylporphyrin-fullerene nanocomposite: a near-infrared light-triggered theranostic platform for imaging-guided photodynamic therapy. *NPG Asia Mater.* **7**, e205 (2015).
- Idris, N. M., Gnanasamandhan, M. K., Zhang, J., Ho, P. C., Mahendran, R. & Zhang, Y. *In vivo* photodynamic therapy using upconversion nanoparticles as remote-controlled nanotransducers. *Nat. Med.* **18**, 1580–1585 (2012).
- Zhao, X. L., Chen, Z. Y., Zhao, H. L., Zhang, D. H., Tao, L. & Lan, M. B. Multifunctional magnetic nanoparticles for simultaneous cancer near-infrared imaging and targeting photodynamic therapy. *RSC Adv.* **4**, 62153–62159 (2014).
- Qiao, Z. & Shi, X. Y. Dendrimer-based molecular imaging contrast agents. *Prog. Polym. Sci.* **44**, 1–27 (2015).
- Wang, Y., Guo, R., Cao, X. Y., Shen, M. W. & Shi, X. Y. Encapsulation of 2-methoxyestradiol within multifunctional poly (amidoamine) dendrimers for targeted cancer therapy. *Biomaterials* **32**, 3322–3329 (2011).
- Zhang, M. G., Guo, R., Wang, Y., Cao, X. Y., Shen, M. W. & Shi, X. Y. Multifunctional dendrimer/combretastatin A4 inclusion complexes enable *in vitro* targeted cancer therapy. *Int. J. Nanomed.* **6**, 2337–2349 (2011).
- Liao, H. H., Liu, H., Li, Y. L., Zhang, M. G., Tomas, H., Shen, M. W. & Shi, X. Y. Antitumor Efficacy of Doxorubicin Encapsulated within PEGylated poly(amidoamine) dendrimers. *J. Appl. Polym. Sci.* **131**, 40358 (2014).
- Torchilin, V. Tumor delivery of macromolecular drugs based on the epr effect. *Adv. Drug Deliv. Rev.* **63**, 131–135 (2011).
- Hu, F. Q., Zhang, Y. Y., You, J., Yuan, H. & Du, Y. Z. pH-triggered doxorubicin delivery of pegylated glycolipid conjugate micelles for tumor targeting therapy. *Mol. Pharm.* **9**, 2469–2478 (2012).
- Win, K. Y. & Feng, S. S. Effects of particle size and surface coating on cellular uptake of polymeric nanoparticles for oral delivery of anticancer drugs. *Biomaterials* **26**, 2713–2722 (2005).
- Fu, Q., Sheng, Y. P., Tang, H. J., Zhu, Z. N., Ruan, M. B., Xu, W. L., Zhu, Y. T. & Tang, Z. Y. Growth mechanism deconvolution of self-limiting supraparticles based on microfluidic system. *ACS Nano* **9**, 172–179 (2015).
- Wang, Y. M., Liu, W. & Yin, X. B. Self-limiting growth nanoscale coordination polymers for fluorescence and magnetic resonance dual-modality imaging. *Adv. Funct. Mater.* **26**, 8463–8470 (2016).
- Bhattacharya, S., Bocker, C., Heil, T., Jinschek, J. R., Höche, T., Rüssel, C. & Kohl, H. Experimental evidence of self-limited growth of nanocrystals in glass. *Nano Lett.* **9**, 2493–2496 (2009).
- Greer, J. R. & De Hosson, J. Th. M. Plasticity in small-sized metallic systems: intrinsic versus extrinsic size Effect. *Prog. Polym. Sci.* **56**, 654–724 (2011).
- Liang, S., Yang, X. Z., Du, X. J., Wang, H. X., Li, H. J., Liu, W. W., Yao, Y. D., Zhu, Y. H., Ma, Y. C., Wang, J. & Song, E. W. Optimizing the size of micellar nanoparticles for efficient siRNA delivery. *Adv. Funct. Mater.* **25**, 4778–4787 (2015).
- Thorek, T. & Tsourkas, A. Size, charge and concentration dependent uptake of iron oxide particles by non-phagocytic cells. *Biomaterials* **29**, 3583–3590 (2008).
- Sur, I., Cam, D., Kahraman, M., Baysal, A. & Culha, M. Interaction of multi-functional silver nanoparticles with living cells. *Nanotechnology* **21**, 175104 (2010).
- Han, J. S., Zhang, J. J., Yang, M., Cui, D. X. & de la Fuente, J. M. Glucose-functionalized au nanoprisms for optoacoustic imaging and near-infrared photothermal therapy. *Nanoscale* **8**, 492–499 (2016).
- Sun, S. H., Zeng, H., Robinson, D. B., Raoux, S., Rice, P. M., Shan X. Wang, S. X. & Li, G. X. Monodisperse MFe<sub>2</sub>O<sub>4</sub> (M=Fe, Co, Mn) nanoparticles. *J. Am. Chem. Soc.* **126**, 273–279 (2004).
- Zhang, Q., Castellanos-Rubio, I., Munshi, R., Orue, I., Pelaz, B., Gries, K. I., Parak, J. P., Pino, D. P., Pralle, A. & Quere, I. Model driven optimization of magnetic anisotropy of exchange-coupled core-shell ferrite nanoparticles for maximal hysteretic loss. *Chem. Mater.* **27**, 7380–7387 (2015).
- Lin, C. A., Sperling, R. A., Li, J. K., Yang, T. Y., Li, P. Y., Zanella, M., Chang, W. H. & Parak, W. J. Design of an amphiphilic polymer for nanoparticle coating and functionalization. *Small* **4**, 334–341 (2008).
- Barriau, E., Pastor-Pérez, L., Berger-Nicoletti, E., Kilbinger, A. F. M., Frey, H. & Stribra, S. E. Systematic investigation of functional core variation within hyper-branched polyglycerols. *J. Polym. Sci. Pol. Chem.* **615**, 2049–2061 (2008).
- Lim, S. F., Zheng, Y. M., Zou, S. W. & Chen, J. P. Characterization of copper adsorption onto an alginate encapsulated magnetic sorbent by a combined FT-IR, XPS, and mathematical modeling study. *Environ. Sci. Technol.* **42**, 2551–2556 (2008).
- Cheng, C. H., Lehmann, J., Thies, J. E., Burton, S. D. & Engelhard, M. K. Oxidation of black carbon by biotic and abiotic processes. *Org. Geochem.* **37**, 1477–1488 (2006).

- 36 Asher, S. A., Lanoul, A., Mix, G., Boyden, M. N., Karnoup, A., Diem, M. & Schweitzer-Stenner, R. Dihedral psi angle dependence of the amide III vibration: a uniquely sensitive uv resonance raman secondary structural probe. *J. Am. Chem. Soc.* **123**, 11775–11781 (2001).
- 37 Hou, W. X., Xia, F. F., Alves, C. S., Qian, X. Q., Yang, Y. M. & Cui, D. X. MMP2-targeting and redox-responsive PEGylated chlorin e6 nanoparticles for cancer near-infrared imaging and photodynamic therapy. *ACS Appl. Mater. Interfaces* **8**, 1447–1457 (2016).
- 38 Yin, T., Huang, P., Gao, G., Shapter, J. G., Shen, Y. L., Sun, R. J., Yue, C. X., Zhang, C. L., Liu, Y. L., Zhou, S. & Cui, D. X. Superparamagnetic Fe<sub>3</sub>O<sub>4</sub>-PEG<sub>2K</sub>-FA@Ce6 nanoprobos for *in Vivo* dual-mode imaging and targeted photodynamic therapy. *Sci. Rep.* **6**, 36187 (2016).
- 39 Lee, N., Cho, H. R., Oh, M. H., Lee, S. H., Kim, K., Kim, B. H., Shin, K., Ahn, T. Y., Choi, J. W., Kim, Y. W., Choi, S. H. & Hyeon, T. Multifunctional Fe<sub>3</sub>O<sub>4</sub>/TaOx Core/Shell nanoparticles for simultaneous magnetic resonance imaging and X-ray computed tomography. *J. Am. Chem. Soc.* **134**, 10309–10312 (2012).
- 40 Li, J. C., Zheng, L. F., Cai, H. D., Sun, W. J., Shen, M. W., Zhang, G. X. & Shi, X. Y. Polyethyleneimine-mediated synthesis of folic acid-targeted iron oxide nanoparticles for *in vivo* tumor MR imaging. *Biomaterials* **34**, 8382–8392 (2013).
- 41 Chan, M. H. & Lin, S. M. Preparation and identification of multifunctional mesoporous silica nanoparticles for *in vitro* and *in vivo* dual-mode imaging, theranostics, and targeted tracking. *Biomaterials* **46**, 149–158 (2015).
- 42 Levy, M., Luciani, N., Alloyeau, D., Elgrabli, D., Deveaux, V., Pechoux, C., Chat, S., Wang, G., Vats, N., Gendron, F. & Factor, C. Long term *in vivo* biotransformation of iron oxide nanoparticles. *Biomaterials* **32**, 3988–3999 (2011).
- 43 Kreyling, W. G., Abdelmonem, A. M., Ali, Z., Alves, F., Geiser, M., Haberl, N., Hartmann, R., Hirn, S., Aberasturi, D. J., Kantner, K., Khadem-Saba, G., Montenegro, J. M., Rejman, J., Rojo, T., Larramendi, I. R., Ufartes, R., Wenk, A. & Parak, W. J. *In vivo* integrity of polymer-coated gold nanoparticles. *Nat. Nanotech.* **10**, 619–623 (2015).
- 44 Yu, J., Hao, R., Sheng, F. G., Xu, L. L., Li, G. J. & Hou, Y. L. Hollow manganese phosphate nanoparticles as smart multifunctional probes for cancer cell targeted magnetic resonance imaging and drug delivery. *Nano Res.* **5**, 679–694 (2012).
- 45 Best, J. P., Yan, Y. & Caruso, F. The role of particle geometry and mechanics in the biological domain. *Adv. Healthcare Mater.* **1**, 35–47 (2012).
- 46 Parkhots, M. V., Knyukshto, V. N., Isakov, G. A., Petrov, P. T., Lepeshkevich, S. V., Khairullina, A. Ya. & Dzhagarov, B. A. Spectral-luminescent studies of the photosensitizer 'photolon' in the model systems and in blood of oncological patients. *J. Appl. Spectrosc.* **70**, 921–926 (2003).
- 47 Frolov, A. A., Arkatov, I. u. M., Gurinovich, G. P., Kochubeev, G. A. & Sarzhevskaya, M. V. Intracellular localization of exogenous photosensitizer-chlorin e6. *Dokl. Akad. Nauk. SSSR* **291**, 715–719 (1986).
- 48 Konan, Y. N., Gurny, R. & Allémann, E. State of the art in the delivery of photosensitizers for photodynamic therapy. *J. Photochem. Photobiol. B* **66**, 89–106 (2002).
- 49 Wang, M. & Thanou, M. Targeting nanoparticles to cancer. *Pharmacol. Res.* **62**, 90–99 (2010).
- 50 Maeda, H., Sawa, T. & Konno, T. Mechanism of tumor-targeted delivery of macromolecular drugs, including the EPR effect in solid tumor and clinical overview of the prototype polymeric drug SMANCS. *J. Control Release* **74**, 47–61 (2001).
- 51 Kam, N. W., Liu, Z. & Dai, H. Carbon nanotubes as intracellular transporters for proteins and DNA: an investigation of the uptake mechanism and pathway. *Angew. Chem. Int. Ed.* **45**, 577–581 (2006).
- 52 Luehmann, T., Rimann, M., Bitterman, A. G. & Hall, H. Cellular uptake and intracellular pathways of PLL-g-PEG-DNA nanoparticles. *Bioconjugate Chem.* **19**, 1907–1916 (2008).
- 53 Florence, A. T., Hillery, A. M., Hussain, N. & Jani, P. U. Nanoparticles as carriers for oral peptide absorption: studies on particle uptake and fate. *J. Control. Release* **36**, 39–46 (1995).
- 54 Sunoqrot, S., Bugno, J., Lantvit, D., Burdette, J. E. & Hong, S. Prolonged blood circulation and enhanced tumor accumulation of folate-targeted dendrimer-polymer hybrid nanoparticles. *J. Control. Release* **191**, 115–122 (2014).



This work is licensed under a Creative Commons Attribution 4.0 International License. The images or other third party material in this article are included in the article's Creative Commons license, unless indicated otherwise in the credit line; if the material is not included under the Creative Commons license, users will need to obtain permission from the license holder to reproduce the material. To view a copy of this license, visit <http://creativecommons.org/licenses/by/4.0/>

© The Author(s) 2017

Supplementary Information accompanies the paper on the NPG Asia Materials website (<http://www.nature.com/am>)